UNIVERSITATEA BABEȘ-BOLYAI
BABEȘ-BOLYAI TUDOMÁNYEGYETEM
BABEȘ-BOLYAI UNIVERSITÄT
BABEȘ-BOLYAI UNIVERSITY
TRADITIO ET EXCELLENTIA

ȘCOALA DOCTORALĂ DE FIZICĂ

BABEȘ-BOLYAI UNIVERSITY
Doctoral School of Physics

The study of morphology and structure of carbon-based materials with potential in electro-analytical applications

-Thesis Summary -

Mihai Marius Rusu

Scientific Advisor:

Prof. Dr. Habil. Lucian Baia

Cluj-Napoca

-2022-

ABSTRACT

The engineering process of nanocomposites is crucial for the progress and innovation for various fields of applications such as catalysis, microfluidic systems, lab-on-chip devices, energetics and sensors. The present thesis outlines the characterization and the early development stages of one such nanocomposite system having potential electrochemical applications such as the detection of heavy metals and/or hydrogen peroxide (H_2O_2). The nanocomposite is based on carbon xerogels (CX) and aerogels (CA) obtained by following a resorcinol-formaldehyde (RF) sol-gel route, while integrating through a co-synthesis approach bismuth (Bi) and iron (Fe) precursors. This approach enables some key aspects such as: conserved monolithic shape, chemical inertness, increased nanoparticle dispersion, control over porous features during synthesis and electron conductive carbon support. The thesis is based on the morphological and structural investigations of the effects induced by the synthesis parameter variations such as the iron precursor concentrations, the drying methods and the pyrolysis conditions. Different techniques are applied such as: X-ray diffraction on powders (XRD), micro-Raman spectroscopy, N_2 adsorption/desorption porosimetry, scanning electron microscopy (SEM) and a set of more advanced methods in transmission electron microscopy (TEM). Valuable results regarding the occurrence of hybrid Bi-O-Fe (BFO) nanoparticles, the nanoparticle growth dynamics and the Fe catalyzed growth of graphitic nanostructures inside the CBiFe xerogel were obtained through: HR-TEM, SAED, CDF, STEM/EDX, in situ TEM combined with image processing tools (segmentation, particle tracking, etc.). The changes induced in the nanocomposite are reflected also by electrochemical methods such as electrochemical impedance spectroscopy (EIS) and heavy metal and hydrogen peroxide detection through square wave anodic stripping voltammetry (SWASV) and amperometry techniques. The correlations observed in the triangle between synthesis, the material properties and electrochemical performances represent the starting point in the development of new sensor platforms.

KEYWORDS: Carbon xerogels, Bi/Fe nanoparticles, graphitization, electron microscopy, nanocomposite characterization, Pb^{2+} detection, H_2O_2 detection

Contents

1. Introduction

Motivations and aims of the thesis

For some, clean water is a luxury, approximately 771 million people do not afford it.[1] Among a vast set of pollutants, heavy metals are found on the priority list of chemical contaminants for current water policies.[2,3] Testing water quality is resource demanding, there is an on-going struggle to develop systems for monitoring the water quality or remediation technologies. Another quest is superposed to this effort – the quest for electrode materials based on nanocomposites for the design of novel sensors that need to satisfy several requirements: high performance for low concentrations, low-cost, disposable, eco-friendly, compatible with miniaturization technologies and so on.

Carbon based materials and composites prove to be ever fascinating and challenging perhaps due to the atomic structure of carbon, its complex allotropes and the vast range of physical and chemical interactions that affect a huge proportion of every system nature and humanity experienced. The carbon xerogels and/or aerogels represent a subclass known among others as a network with tunable pores and as a vitreous, electron-conductive environment with high surface areas. These materials are obtained through a resorcinol-formaldehyde (RF) sol-gel synthesis followed by drying and pyrolysis. In the past twenty years, the incorporation of metal salts into the synthesis pathway has led to the formation of nanocomposites with relevant results in energy storage, heavy metal detection techniques, magnetic adsorbents, filters and "gas reduction" devices. From this wide palette, bismuth and iron doped carbon gels are considered as potential electrode materials used for the electrochemical analysis of aqueous environments.[4–9] Bismuth is considered as one of the most efficient and non-toxic compounds currently used for the electrochemical detection of heavy metals,[10] also showing sensitivities towards biological compounds such as glucose.[11] In addition to the roles of graphitizing catalysts or magnetic centers, iron based nanoparticles (metallic or oxide) were also reported to electrochemically detect various compounds related with biological processes i.e. hydrogen peroxide,[12] glucose,[13] warfarin,[14] paracetamol.[15]

One other factor that enforces this pursuit is the awareness of our daily exposure to various types of distress factors such as heavy metals, pesticide or radioactive contaminants, air pollutants and the contraction of various diseases and from the other point of view, the lack of both powerful and accessible technologies that can detect, diagnose or even counteract their harmful effects. Considering the example of increased exposure of biological systems to heavy metal contaminants (Pb^{2+}, Cd^{2+}, Hg^{2+}, etc.), it was shown that such distress factors can trigger complex oxidative stress processes in various biological systems, affecting the balance between the production of active oxygen species (O_2^{-}, $^1O_2$, $OH^{\cdot}$ and H_2O_2) and the counteractive enzymatic antioxidant systems.[16–19] An intriguing approach could be related to the development of a nanocomposite material that may detect both distress input factors (i.e. heavy metal species) and output effects (i.e. H_2O_2 activity) in order to collectively aid such applications, and to also consider requirements novel sensors need to fulfill as mentioned earlier.

The current study follows the assumption that tailoring an initial RF sol-gel synthesis process by simultaneously integrating components such as Bi and Fe precursors may add multi-

functionality for addressing a wider repertoire of applications. In this context, the characterization of new materials and nanocomposites and the impact the variation of synthesis parameters will influence their performance represents one of the most valuable interfaces that may catalyze progress from the preliminary synthesis stages towards optimal solutions and real applications.

The first objective consisted in the design of nanocomposite material with a fairly simple and low-cost production that can effectively be applied in heavy metal sensing applications, as well as H_2O_2 detection. The second objective is central to the present thesis, namely, to characterize the novel nanocomposites in terms of composition, morphology and structure and to evaluate the relations between synthesis parameters, material parameters and electrochemical performance as electrode materials. The third objective was to investigate the Fe assisted graphitization activity in such nanocomposites, which was considered to potentially enhance the electrode performance due to improved charge transport properties.

Thesis structure and outline

Chapter 2 introduces resorcinol-formaldehyde sol-gel synthesis as sub-branch of the carbon family, further focusing on the historical aspects and synthesis steps. The second part of the chapter is treating nanocomposite materials derived from the RF sol-gel and adjacent protocols. The chapter ends with the literature overview on the heterogeneous graphitization mechanism found in different carbon systems, including resorcinol-formaldehyde derived carbons. **Chapter 3** briefly summarizes the main characterization tools used for vitreous carbon materials and their derived nanocomposites in terms of composition, structure and morphology. Further on, the electrochemical techniques that were used during the present studies are briefly introduced. **Chapter 4** presents the experimental details for the synthesis, characterization and electrode studies specific for the present systems. The morphological and structural analysis of a "binary" C-Bi xerogels and aerogels is presented in **Chapter 5**. The effect of iron addition during the co-synthesis and impregnation of "ternary" C-Bi-Fe nanocomposites is treated in **Chapter 6**. In **Chapter 7**, a highly graphitized CBiFe sample is compared with its non-graphitized aerogel variant and with non-graphitized powdered and monolithic xerogel variants. **Chapter 8** follows the temperature dependent evolution of the morphology and structure of one CXBiFe composite by using TG/DTG/DTA and real-time *in situ* TEM investigations. This represents one of the cornerstones of the present study, as it enables the classification of the morphological and structural features into several stages and provides helpful feedback regarding the system dynamics and graphitization mechanism. **Chapter 9** presents a systematic study on the effects of pyrolysis parameters emerged at nano-scales. The analysis continues in **Chapter 10** where the CXBiFe monolithic structures are further investigated at micro-scales. **Chapter 11** ends the experimental part with a summary over the electrochemical results obtained for glassy carbon electrodes modified with chitosan and a set of the CBi and CBiFe nanocomposites. The results emphasize their general applicability as sensing materials for the electrochemical detection of heavy metals (Pb^{2+}) and bio-markers (H_2O_2). Finally, the most relevant findings and the limits of the current study, in parallel with several on-going research directions are presented in the final **Chapter 12**.

2. Carbon xerogels and aerogels derived from resorcinol-formaldehyde. Nanocomposite systems

2.1. Historical and research perspectives for carbon xerogels and aerogels

Perhaps one of the first highly porous organic RF based materials were initially reported by Pekala et al..[22] Their extensive research on RF and carbon aerogels revealed important relations between different synthesis parameters, such as the resorcinol-catalyst ratios (R/C), solid/solvent dilution, type of precursor and pyrolysis temperature with their final morphology and structure.[23] In tandem, effects of their specific ultrastructure over various physical properties such as their mechanical properties,[23] thermal conductivity[24] electric transport mechanisms,[25,26] and their electrochemical behavior[27,28] were investigated. Different applications such as supercapacitors,[29] deionization[30] and environmental clean-up[31] were highlighted as potential applications of the carbon aerogel. The ability to combine the properties of carbon networks with other nanoparticle systems later bloomed the research interest in carbon gels and nanocomposites from the 2010-2020 and currently expanding. The later trends are focused on (1) new 3D network architectures based on different carbon feedstock, also including carbon nanotube or graphene-based gels, (2) complex organic/carbon-inorganic nanocomposites,[32] (3) hetero-atom doping of carbon gel structures,[33] patterning and miniaturization,[34,35] as well as improving mechanical strength and resilience.[36,37]

2.2. The synthesis of carbon xerogel and aerogel materials

The primary resorcinol-formaldehyde reactions

According to recent studies,[38] the synthesis of resorcinol-formaldehyde derived carbon networks consists in a complex multi-stage process described in **Figure 2-1**. The main phenomena that lead to the gel-like morphology consist in: (1) catalyst assisted dimerization/oligomerization of precursors, (2) fast exothermal R-F bridging/addition reactions and (3) a temperature dependent crosslinking or network formation through poly-condensation. The role of the catalyst (most frequently Na_2CO_3, as well as other metal salts during nanocomposite co-synthesis[39]) is to transfer electrons to resorcinol so that hydroxymethyl derivates of resorcinol are obtained, followed by further connections with adjacent groups only to form the primary clusters.[23] The clusters, further referred to as basic structural units (BSU), have a spheroidal shape, while their size and connectivity is strongly influenced by multiple synthesis variables.

The polymerization stage

Once the BSU are formed, the cross-linking reactions between the individual BSU can be initiated. Due to the endothermal nature of the crosslinking reaction, a typical synthesis requires the sol to be sealed and heated for several hours at temperatures between 40-80 °C (depending on the solvent and pH).[39] According to the literature, the mechanisms through which the gel state is reached are predominantly based on a microphase separation (associated with spinodal decomposition) and secondary on kinetic growth mechanism (associated with nucleation and cluster growth).[38,40] The gelation time depends on pH and temperature and usually ranges between 1-7 days. The resulting product is termed “sol-gel”, as a polymerized network (gel) is filled with unreacted liquid (sol).

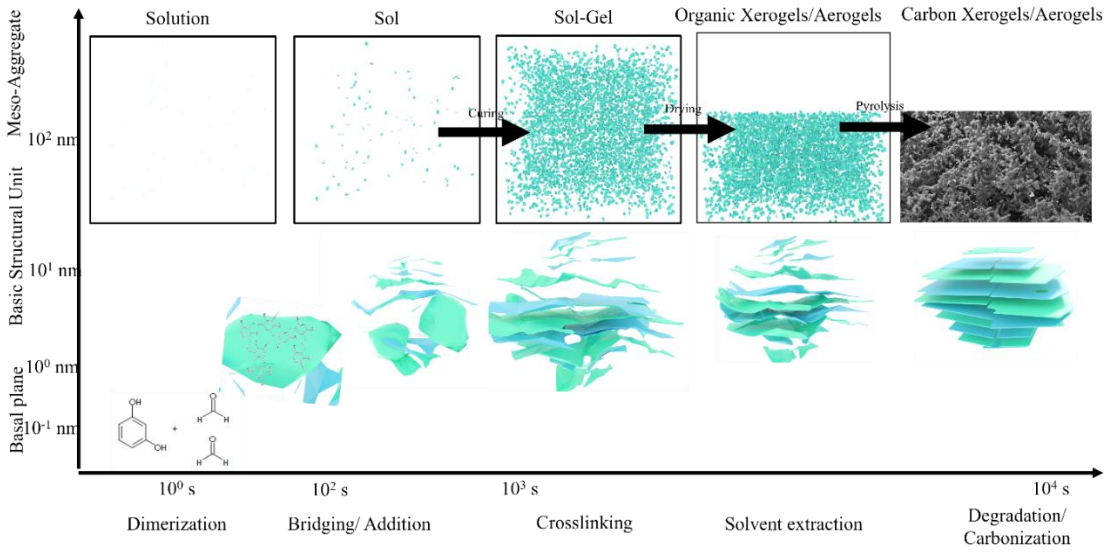

Figure 2-1. Synthesis stages for RF derived carbon xerogels/aerogels

Drying processes

After crosslinking, the sol-gel compound follows a drying stage, during which the liquid phase extraction will fundamentally impact the pore network structure. By undergoing an ambient drying, "xerogels" result having low porous features due to the large capillary forces that collapse the pore network. In order to minimize crack formation or destruction of the monolithic state of the sample, a solvent exchange step can be applied in order to replace water with a fast evaporating solvent (i.e. ethanol) miscible with the supercritical drying fluid (i.e. CO_2). The aerogel morphology is obtained, after solvent exchange, by applying a supercritical drying process.

Pyrolysis processes

The main role of the pyrolytic thermal treatments is to convert the RF derived polymer into an electron conducting carbon network, a highly important aspect that concerns their performance as electrode materials. During this process, structural and morphological transformations take place: (1) the polymer clusters are converted into vitreous carbon BSU, (2) densifications of the carbon support take place typically at micro-pore scales (around 1-2 nm).[41]

2.2. Electrode materials for sensing applications based on RF derived nanocomposites

Binary C-Bi nanocomposites

During the last decades, bismuth materials were introduced as bio-friendly electrode materials that can successfully substitute the active role played by mercury in electrochemical stripping analysis for heavy metal trace detection.[42] This is mainly due to its ability to form "fusible alloys" with other metals such as Hg, Pb, Cd, Zn, etc. Reports indicate electrochemical performances comparable with mercury-based systems (low background, wide potential window), while also revealing low oxygen interference, improved mechanical stability, while profiting from other advantages as well: real-time, on-site measurements, good sensor response in terms of limits of detection, sensitivity and range of detectable analytes.[48,49] One challenge is to further reduce the

amount of bismuth required for electrode production, while maintaining high performance levels.[43] This can be exploited as C-Bi nanocomposites, by dispersing the bismuth as nanoparticles with large electrochemical area.

Binary C-Fe nanocomposites

The last century also opened new directions such as Fe catalyzed Fischer-Tropsch reactions and the use of metal nanoparticles (Ni, Fe, Cr, etc.) in the production of carbon nanostructures. Iron nanoparticles are also investigated as electrochemically active sensors for bio-related compounds such as H_2O_2,[12,20] glucose,[53] dopamine.[44] Due to their time stability and lower cost, they may represent a more advantageous alternative to the classic peroxidase enzyme-based sensing systems or other more costly metal nanoparticle approaches based on noble metals.

2.3. RF derived carbons and the heterogeneous graphitization mechanism

RF derived carbon gels are hard carbons, meaning that they cannot spontaneously graphitize until reaching temperatures above 2000 °C. Efforts are continuously made to further improve their electric conductivity. One trend refers to the direct integration of carbon nanostructures, i.e. carbon nanotubes,[45] graphene,[46] etc. into RF derived carbon gels. However nanostructured carbon additives may add complexity to the system while also increasing production costs. The metal assisted heterogeneous graphitization (HG) of the RF gels, thus represented a promising alternative.

Mechanisms of heterogeneous graphitization

The metal assisted graphitization mechanism can be understood using Vapor-Liquid-Solid (VLS) and/or Vapor-Solid-Solid (VSS) models described in several steps: (1) temperature assisted activation of catalyst nanoparticle, (2) dissolution of carbon species from the external C source or feedstock (that can be found in gaseous, liquid or solid states), (3) adsorption on the catalyst surface, (4) molecular cracking of carbon feedstock, (5) surface/bulk diffusion and catalyst saturation with carbon forming a quasi-stable metal carbide phase followed by (6) carbon precipitation as lower entropy structures such as graphene sheets, nano-onions, -coils, -fibers or -coaxial tubes. During early studies, metals were classified after their catalytic graphitization efficiency.[47] Bismuth was one of the poorly graphitizing metals (among Ca, Pb, Cd, Zn, Al, Si), while Fe is one of the most efficient (among Ni, Cr, V, Ti and Co).[47] The main challenge in reaching a high efficiency of the heterogeneous graphitization is that it depends on a high number of variables such as: temperature, type of catalyst, type of feedstock, pyrolysis atmosphere conditions, thermal changes in morphology and structure of catalyst, etc.

Contributions added by the research group during the present thesis

During the present PhD stage, our research group investigated the perspectives of merging the C-Bi and C-Fe nanocomposites into a multifunctional C-Bi-Fe material by using a simple one-pot sol-gel synthesis.[5,7–9] We initially demonstrated that such systems can detect both heavy metals (Pb^{2+}) and bio-markers (H_2O_2).[7] The following reports were based on the effects induced by varying the initial iron concentrations[9] and the pyrolysis conditions.[8] The HG mechanisms were investigated in ternary C-Bi-Fe nanocomposites, emphasizing the role of the pyrolysis conditions, and the strong link with efficiency of catalyst activation.[8] To our knowledge, these were the first studies reported on sol-gel derived C-Bi-Fe systems also showing good performance as heavy metal and H_2O_2 sensitive materials and a deep insight on the graphitization activity occurring under certain conditions.

3. Nanocomposite characterization tools

3.1 X-ray diffraction technique (XRD)

3.2 Micro-Raman spectroscopy for carbon materials and nanocomposites

3.3 N_2 adsorption method

3.4 Scanning electron microscopy (SEM)

3.5 Transmission electron microscopy (TEM)

3.6 Electrochemical impedance spectroscopy (EIS). Square wave anodic stripping voltammetry (SWASV) and amperometry.

4. Experimental design and characterization

4.2 Nanocomposite synthesis

The modified sol-gel synthesis route used for the preparation of binary and ternary nanocomposites is described as follows:[5,9] mainly $Bi(NO_3)_3 \cdot 5H_2O$ (1.20 g, 2.47 mmol) and resorcinol (2.00 g, 18.17 mmol) are dissolved into glycerol formal (10 mL) at room temperature under stirring conditions. Formaldehyde is then added to the homogeneous solution by fixing the R/F molar ratio to 0.5 throughout the entire set of experiments. Ammonium hydroxide (10%, 4 ml) and glacial acetic acid (12 mL) are finally introduced. For ternary CBiFe nanocomposites, the iron acetate (0.01-1.2 g) will represent the final precursor added to the mixture. After a 10 min stir, the solution is transferred into cylindric glass vial, sealed and cured at 60 °C for 72 h. The resulting organic gels are further rinsed with acetic acid and ethanol.

The drying of the gels consists either in an ambient drying procedure (exposure to air at room temperature for 3 days) to obtain a xerogel morphology or CO_2 supercritical drying to yield aerogel morphologies. The pyrolysis treatments were performed in quartz tube furnaces at various temperatures, usually including a pretreatment at 250-450 °C.

4.3 Characterization methods

X-ray diffraction (XRD) measurements were performed using a Shimadzu 6000 diffractometer equipped with Cu-Kα radiation source (λ = 1.5406 Å) and a graphite monochromator.

Nitrogen adsorption/desorption measurements at 77 °K were performed using a Sorptomatic ADP (Thermo Electron Corp.) equipment after degassing around 100 mg of the tested material for 20 h at 102 °C in a vacuum (<1 mPa). The specific surface area was determined using the 3 parameter BET (Brunauer–Emmet–Teller) method and the pore size distribution and the cumulative pore volume were evaluated using the BJH (Barret–Joyner–Halenda) method

performed on the desorption isotherm. The cumulative micropore volumes and estimated micropore diameter were determined using the HK (Horvath-Kawazoe) method.

For Raman spectroscopic investigations, a Renishaw in Via Reflex Raman Microscope equipped with a Ren Cam CCD detector was used. The spectra were acquired using 532 nm laser line and objectives of various magnifications (20 x – 100 x). The integration times varied between 10-30 s, and the laser power was 1 mW in order not to damage the samples. The Raman spectra were recorded with a spectral resolution of 4 cm^{-1}.

For SEM investigations, A FEI Quanta 3D FEG dual beam – in high vacuum mode using EDT (Everhart Thornley Detector) Scanning Electron Microscope (equipped with an ApolloX SDD Energy Dispersive X-ray (EDX) detector) was used for investigating the surface and elemental composition of the pyrolyzed monoliths.

Transmission electron microscopy (TEM) was performed on the grinded samples dispersed in water or ethanol. The micrographs acquired in bright field (BF), conical dark field (CDF), high resolution (HRTEM) and HAADF-STEM modes together with selective area electron diffraction patterns (SAED) were acquired using FEI Tecnai G^2 F20 X-Twin TEM operating at 200 kV.

Advanced TEM investigations were performed during a research internship at Ecole Polytechnique, Palaiseau, France. A Cs corrected Titan-Themis (operating at 200 kV) was used for HAADF-STEM imaging and broad range elemental analyses using a SuperX detector. The in situ heating experiments were performed using a Cs image corrected Titan environmental transmission electron microscope (ETEM), at a 300 kV operating voltage and equipped with an UltraScan 2k x 2k CCD camera and a direct electron K2 camera. The samples were dispersed on the surface of specific heating membranes with SiN_x windows and mounted on a Protochips Fusion sample holder. More details are provided elsewhere.[8]

The thermal analysis (TG-DTG-DTA) was performed using a NETZSCH STA 409 PC/PG equipment. The powdered organic xerogel was placed in an alumina crucible and heated at 1100 °C using 10 °C/min heating rate, under N_2 stream (0.5 mL/min).

4.4 Electrode preparation and electrochemical tests

Prior to electrochemical tests, glassy carbon electrodes (GC, geometrical area of 0.07 cm^2) are polished with alumina slurry (1 μm, and then 0.1 μm Stuers, Copenhagen, Denmark). The alumina particles and any other contaminants are removed by washing the GC surface with with bi-distilled, followed by a 5 min sonication in acetone bath.
Then a chitosan (Chit) solution is prepared: 10 mg Chit are dissolved into 10 mL of 0.1 M acetic acid. Then, a constant amount of CBi/CBiFe nanocomposite (1 g/L) is added. The mixture is sonicated for 2 h. Finally, a 5 μL drop of the suspension is immobilized onto GC and dried under a beaker for 2 h at room temperature.

The electrochemical measurements were performed with a PC controlled electrochemical analyzer (AUTOLAB PGSTAT302N EcoChemie, Utrecht, Netherlands). A three-electrodes cell was used: the modified electrode was used as working electrode, a Pt wire, as counter electrode, and $Ag/AgCl,KCl_{sat}$ as reference electrode. Further details are presented elsewhere.[5–7,9,20]

5. Binary CBi nanocomposite systems – Xerogels, aerogels and modified electrodes

5.1 Introduction

The effects of the drying stage over the composition, morphology and structure of the CBi nanocomposite xerogel and aerogel monoliths is analyzed in the present chapter. The samples were obtained using the co-synthesis approach. The synthesis variables are presented in **Table 5-1**.

Table 5-1. Experimental details for the investigated high temperature CBi samples

	Sample	Synthesis	$Bi(NO_3)_3 \cdot 5H_2O$ [g]	Drying and processing	Pyrolysis conditions
1	X_{CBi}	Co-synthesis	1.2	Xerogel, monoliths	Purge gas: Ar Pretreatment: 250 °C, 2 h Pyrolysis: 750°C, 2h
2	A_{CBi}			Aerogel, monoliths	

5.2 Drying and the porosity of nanocomposites

The adsorption and desorption isotherms presented in **Figure 5-1** indicate that the X_{CBi} and A_{CBi} adsorption isotherms are compact microporous and predominantly mesoporous materials, respectively.[48] In **Table 5-2**, the main morphological and structural parameters are summarized. SEM and TEM investigations supplement the previous findings (**Figure 5-2**): as observed, the xerogels exhibit some microporous features, while the aerogels reveal a hierarchical pore structure including the macro-pore class as well.

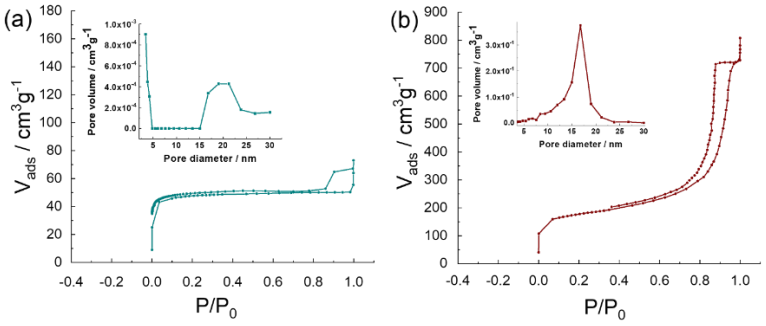

Figure 5-1. N_2 adsorption data obtained for (a) X_{CBi} and (b) A_{CBi} samples

Table 5-2. Morphological and structural parameters of CBi xaerogel and aerogel samples

Sample	S_{BET} (m^2/g)	V_{meso} (cm^3/g)	D_{meso} (nm)	V_{micro} (cm^3/g)	D_{micro} (nm)	C/O/Bi (at%)		
X_{CBi}	149	0.03	17	-	-	95.9	3.2	0.9
A_{CBi}	570	1.012	14	0.29	2	95.9	2.7	0.5

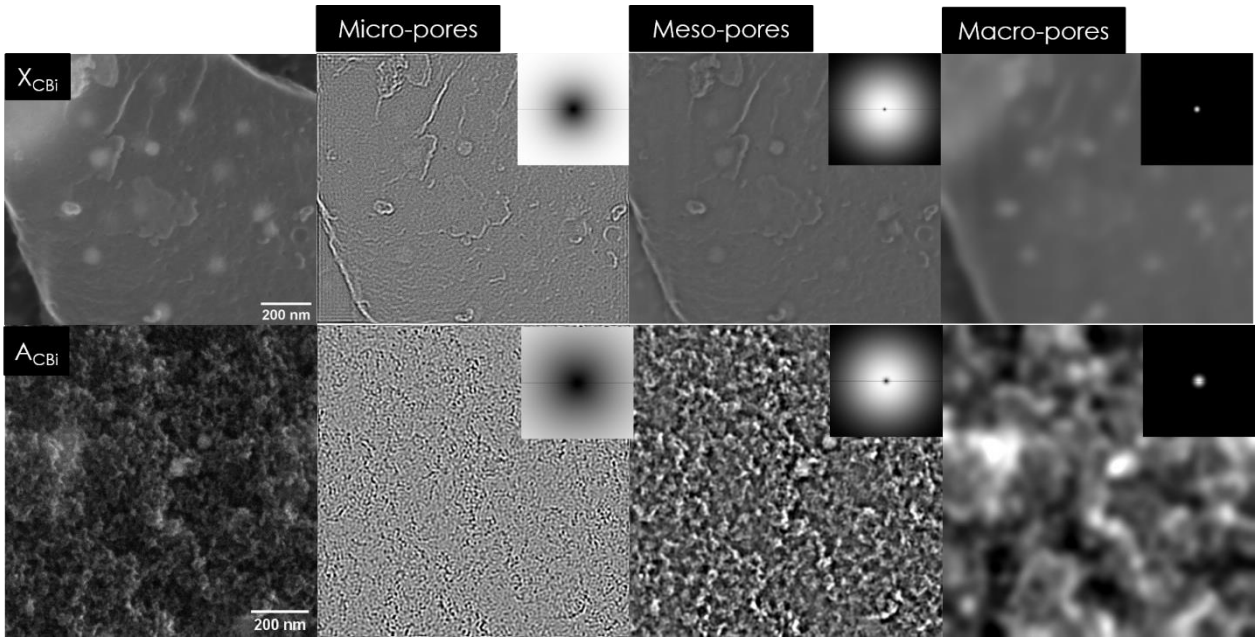

Figure 5-2. Spatial frequency domains from SEM micrographs acquired for samples X_{CBi} and A_{CBi} correlated with the presence of micropores, mesopores and macropores. The insets indicate with white the portions from the FFT of the SEM micrographs selected for the iFFT reconstruction

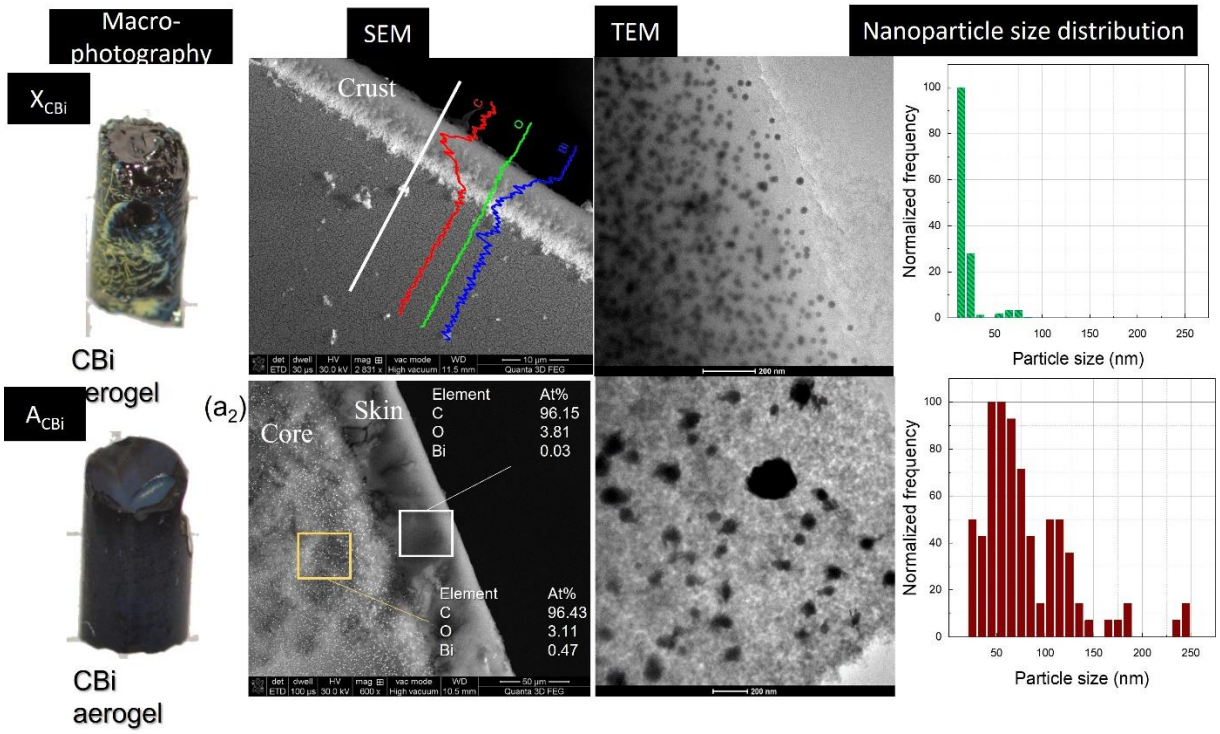

Figure 5-3. Features observed from monolith lateral view at low magnifications, the transversal edge and the core of the X_{CBi} / A_{CBi} nanocomposites using SEM/EDX, TEM and TEM derived Bi nanoparticle size distribution.

5.3 Migration of bismuth phase at multi-scale

The distribution of the bismuth component into such composites was analyzed at (1) the external crust of the monoliths and (2) at the core as presented in **Figure 5-3**. For the X_{CBi} sample, the external crust is composed of Bi rich structures, while the external region of A_{CBi} is rather a carbon based . At large scales, a homogeneous distribution of Bi based nanoparticles is evidenced across the monolith. For the xerogels, the presence of nanoparticles is clear only at larger magnifications. The EDX quantifications (**Table 5-2)** indicate that the X_{CBi} monolith exhibited higher Bi concentrations compared to A_{CBi} both in the core and the mantle of the monoliths.

As observed in **Figure 5-4**, the TEM results confirm that the carbon support is collapsed into a compact structure having embedded Bi nanoparticles with a spheroidal shape. The nanoparticles exhibited a bimodal size distribution, as depicted in **Figure 5-4a**. For X_{CBi}, the primary mode being centered at 25 nm and the secondary around 110 nm (the observed dimensional range was 2-170 nm). For the A_{CBi} sample, the size distribution is broader: nanoparticle diameters were recorded roughly between 20 and 370 nm, with clear deviations from spherical geometry. The bi-modal nature is roughly maintained, with two maxima at 60 nm and 120 nm.

5.4 Effects over the crystalline features

The structural features of X_{CBi} and A_{CBi} samples were analysed through XRD, HRTEM and Raman spectroscopy. For the X_{CBi} sample, a two-phase mixture of β-Bi_2O_3 and metallic Bi is observed, while for sample A_{CBi}, β-Bi_2O_3 and $(BiO)_2CO_3$ are more clearly observed through XRD. The Raman spectra, represented by the regions ascribed initially to the D and G bands, indicate similar features (the $I_D/I_G \sim 0.89$). A broadening effect of D and G regions is observed for A_{CBi}, that may indicate increased levels of disorder and higher surface contributions.

5.5 Conclusions

The results confirm that by subjecting the sol-gel system to an ambient drying, the pore structure collapses leading to shrinkage, macroscopic cracks, and a significant loss in pore volume and specific surface area.

The SEM analysis of the monolith samples suggest that the high capillary forces developing on the pore walls during ambient drying will drive the sol mixture towards the external part of the monolith, favoring the formation of a metal rich crust at the xerogel surface. This effect is maintained for similar nanocomposite xerogels and will be further discussed for ternary CBiFe systems in the next chapters. For the CBi aerogel, the solvent exchange and supercritical drying will conserve the pore network structure, while preventing the formation of metal/oxide layer on the surface due to purging the CO_2/sol mixtures outside the system. This will lead to monoliths with more homogeneous aspect but also to losses in Bi concentrations. As observed from the SEM/TEM results, the pore network structure will influence the growth process of the Bi nanoparticles. Due to large surface area and a well-connected pore network of the aerogel, mass transport of the Bi component is improved, and larger nanoparticles, aggregations and higher inter-distances are confirmed within the aerogel monolith.

6. Ternary CBiFe composites with variations in iron concentration

6.1 Introduction

The chapter is based on the analysis of the effects induced by the Fe content over morphology and structure in three CBiFe sample batches obtained through co-synthesis (aerogels treated at 1050 °C and xerogels treated at 750°C) and co-synthesis followed by impregnation (xerogels treated at 1050°C). The experimental details for the synthesis of the samples are presented in **Table 6-1**.

The aerogel samples (batch CABiFe0-3) revealed very low contributions of the Bi phases, while the xerogels exhibited both Bi and Fe metal-oxide phases. The samples resulting from a co-synthesis, followed by impregnation and pyrolysis at 1050 °C under Ar (sample A1050_imp) and N_2 flow (sample N1050_imp) also indicate small bismuth contributions. Further details are provided here only for the xerogel samples treated at 750 °C under N_2 (batch CXBiFe0-3)

Table 6-1 – The parameters varied during the synthesis of CBiFe nanocomposites with different Fe concentrations

	Sample	**Synthesis**	**$Fe(OAc)_2$ amount [g]***	**Drying and processing**	**Pyrolysis conditions**
CBiFe aerogel samples					
1	CABiFe0	Co-synthesis	0.00	Aerogel, monolithic chunks	Purge gas: Ar Pretreatment: 250 °C, 2 h Pyrolysis: 1050°C, 1h
2	CABiFe1		0.01		
3	CABiFe2**		0.06		
4	CABiFe3		0.12		
CBiFe xerogels samples					
5	CXBiFe0	Co-synthesis	0.00	Xerogel, monolithic chunks	Purge gas: N_2 Pretreatment: 250 °C, 2 h Pyrolysis: 750°C, 1h
6	CXBiFe1		0.01		
7	CXBiFe2		0.12		
8	CXBiFe3***		1.2		
11	A1050_imp	CXBiFe2 +Impregnations	0.06 g (+ 0.1 M)		Purge gas: N_2 Pretreatment: 250 °C, 2 h Pyrolysis2: 1050°C, 1h
12	N1050_imp		0.06 g (+ 0.1 M)		Purge gas: Ar Pretreatment: 250 °C, 2 h Pyrolysis2: 1050°C, 1h

*The other synthesis parameters were kept constant. (i.e. the R:C, R:F ratios and the $M_{Bi(NO3)3}$=1.2g precursor amount),
** Prototype for samples in **Chapter 7**, ***Prototype for samples treated in **Chapters 8-10**.

6.3 CBiFe xerogels obtained through co-synthesis

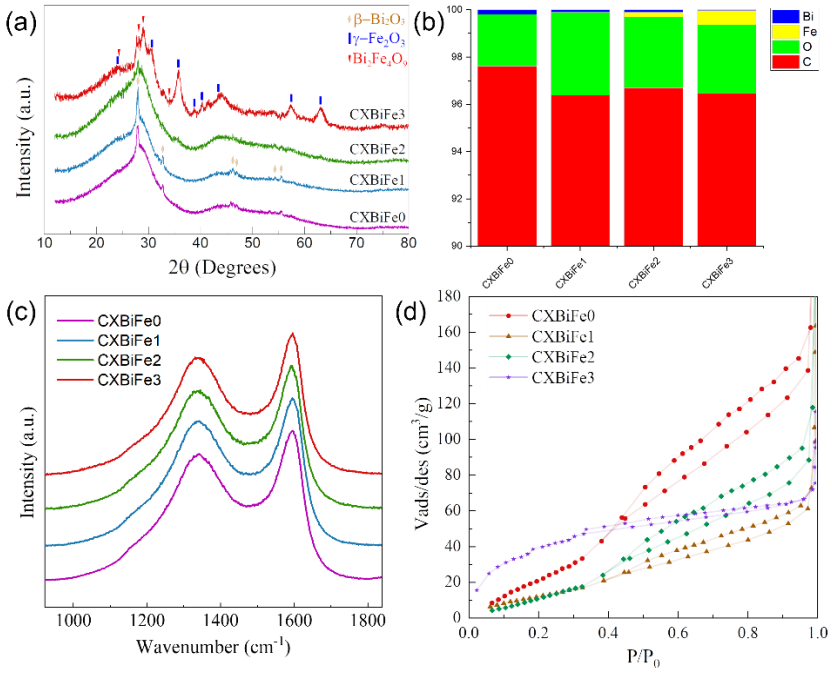

Figure 6-1 - Effect of different Fe concentrations in CBiFe xerogel nanocomposites after pyrolysis at 750 °C: (a) the XRD patterns, (b) the elemental composition (at %) derived from SEM-EDX spectra quantifications, (c) Raman spectra, (d) N_2 adsorption/desorption isotherms

The recorded XRD patterns are presented in **Figure 6-1a**. In addition to the two vitreous carbon signals, another broad signal is observed at about $2\theta = 30°$, that was attributed to amorphous bismuth oxide. The crystalline peaks of the tetragonal Bi_2O_3 phase are most visible for CBiFe composites low in Fe content. An amorphization of the Bi_2O_3 and signals tracing to Fe_3O_4 / γ-Fe_2O_3 is observed at higher iron concentrations. The additional signals observed for CXBiFe3 at 2θ = 28.2 and 29.0° were ascribed to a $Bi_2Fe_4O_9$ phase. The elemental composition of the investigated nanocomposites (**Figure 6-1b**) confirms the increase in Fe at %. It is important to note that higher Bi contributions were observed in comparison with CABiFe0-3 batch. Oxygen contributions were also lower. In the Raman spectra of the CXBiFe nanocomposites (**Figure 6-2c)**, the graphitization yield, expressed as I_D/I_G ratio, does not indicate any clear differentiation between the samples. The results indicate that the Fe assiste graphitization mechanisms may be active only at a small extent. The N_2 adsorption/desorption isotherms presented in **Figure 6-2d** indicate Type III adsorption isotherms at low Fe concentrations (specific to weak adsorbate-adsorbent interactions)[48], while a Type I isotherm is observed for sample CXBiFe3. The desorption branches describe a H3-H4 hysteresis, specific to slit shaped pores in mesoporous and microporous systems. The S_{BET} parameter varies non-monotonously with Fe concentration: from the S_{BET}= 185 m^2/g obtained for CXBiFe0, the values decrease to S_{BET}= 65 m^2/g for CXBiFe1, then increase to 79, for CXBiFe2, and 162 m^2/g, for CXBiFe3. This correlates with an increase in the micropore volumes, while the mesopore volume possess an opposite trend.

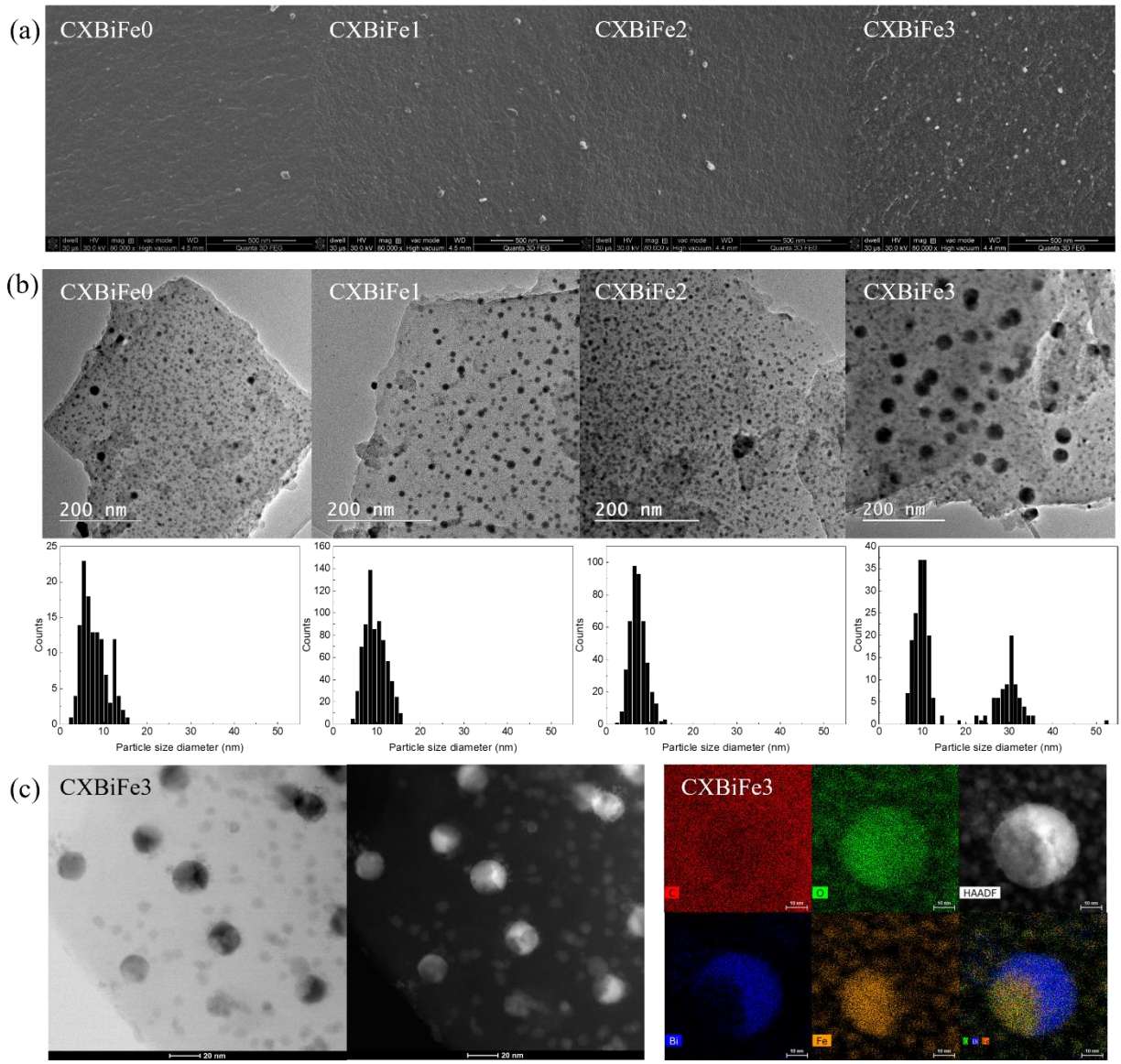

Figure 6-2 – Electron microscopy investigations of CBiFe nanocomposites with varied Fe concentrations: (a) SEM micrographs (at 8000x), (b) TEM and TEM derived particle size distributions for all investigated samples and (c) observations of BFO hybrid nanoparticles through STEM-BF, STEM- HAADF and STEM-EDX. The chemical maps indicate the distribution of elemental carbon (red), oxygen (green), bismuth (blue) and iron (orange)

The results of the two SEM and TEM electron microscopy analysis indicate that by increasing the Fe concentration, a trend of increase in average nanoparticle size is obtained (**Figure 6-3b**). Apparently, the sample CXBiFe3 exhibits a bimodal size distribution, a secondary mode around 30 nm in the size histogram, confirmed by TEM analysis. Interestingly, when analyzing the larger nanoparticles in STEM-HAADF and STEM-EDX, the nanoparticles reveal a hybrid structure (**Figure 6-3c**). A heterogeneous distribution of the Bi and Fe elements is also confirmed by STEM-HAADF and EDX maps. Thus, Fe_2O_3 regions, may act as anchoring sites for the Bi fraction, also explaining the size increase observed at higher Fe concentrations. In contrast with CXBiFe0, the CXBiFe1-4 samples will contain Fe modified Bi surfaces. This may alter both their electrochemical response and graphitization activity.

6.5 Conclusions

The aerogel samples having different Fe concentrations revealed very low contributions of the Bi phases (treatment at 1050 °C), while the xerogels exhibited both Bi and Fe metal-oxide phases (treatment at 750 °C). For the xerogel sample batch, Bi-O-Fe interactions were highlighted during XRD and TEM/STEM investigations as $Bi_2Fe_4O_9$ mullite phases and peculiar BFO hybrid nanoparticles were observed. No sign of graphitization activity and no significant changes to the Raman D and G bands specific to carbon were observed. N_2 adsorption measurements performed on the xerogels indicate microporous features and larger BET surface areas obtained with the increase in Fe content.

The gel resulting from a co-synthesis pathway having an intermediate iron concentration was further enriched with iron through an impregnation route, dried under ambient conditions and then pyrolyzed at 1050 °C under Ar and N_2 flow to obtain different reduction yields. According to the sample analysis, more reactive conditions are obtained in the N_2 atmosphere that will tend to affect both the carbon supports and the reduction state of the embedded nanoparticles. The XRD and XPS analysis reveal a mixture of Fe phases (metallic and oxide states). The dominant phase found in the Ar treated sample was ascribed to hematite. The dominant phase found in N_2 treated samples was ascribed to maghemite. The presence of Fe catalyzed graphitic structures was confirmed during the TEM investigations, while the micro-Raman and XRD investigations could not emphasize the graphitized phase, implying the graphitization activity is found in an incipient stage.

7. High temperature CBiFe: between graphitization, drying and mechanical processing

7.1 Introduction

After analyzing the effects induced by the changes in Fe precursor concentrations during the sol-gel process, the present investigation is focused on how the drying parameters (ambient drying versus supercritical drying) and the mechanical processing of samples as powders or monoliths will affect the morphology and structure at high temperature CBiFe nanocomposites (see experimental details given in **Table 7-1**). The most interesting sample represents one CXBiFe xerogel powder pyrolyzed at 1050 °C for 1h under N_2 purge that revealed high graphitization activity (sample G).[8]

Table 7-1. Experimental details for the investigated high temperature CBiFe samples

	Sample	**Synthesis**	**$Fe(OAc)_2$ amount [g]**	**Drying and processing**	**Pyrolysis conditions**
1	A2M	Co-synthesis	0.06	Aerogel, monolithic chunks	Purge gas: Ar Pretreatment: 250 °C, 2 h Pyrolysis: 1050°C, 1h
2	X2M			Xerogel, monolith	
3	X2P			Xerogel, grinded	
4	G			Xerogel, grinded	Purge gas: N_2 Pretreatment: 250 °C, 2 h Pyrolysis: 1050°C, 1h

7.2 Morphological and structural effects induced by drying and powder processing over high temperature CBiFe nanocomposites

The XRD patterns of the investigated nanocomposites are presented in **Figure 7-1a**. As before, the presence of the vitreous carbon phase, marked by the broad signals centered at 2θ = 20.5° and 2θ = 44°, respectively is best evidenced for samples A2M and X2P. The region found between 2θ = 40° and 50° is representative for the (100)/(101) graphitic reflections marking the ordered array of atoms found in the basal plane of the BSUs. The iron phases, γ-Fe_2O_3 and γ-Fe, are also observed in the diffraction patterns of samples X2M and G. However, the γ-Fe phase was not evidenced in the sample X2P. The strong reflection observed at 2θ = 25.75° found in sample G is attributed to the (002) stacked graphitic planes. No significant Bi/Bi_2O_3 phases were detected, except for the X2M monolith, where a metallic Bi phase dominates.

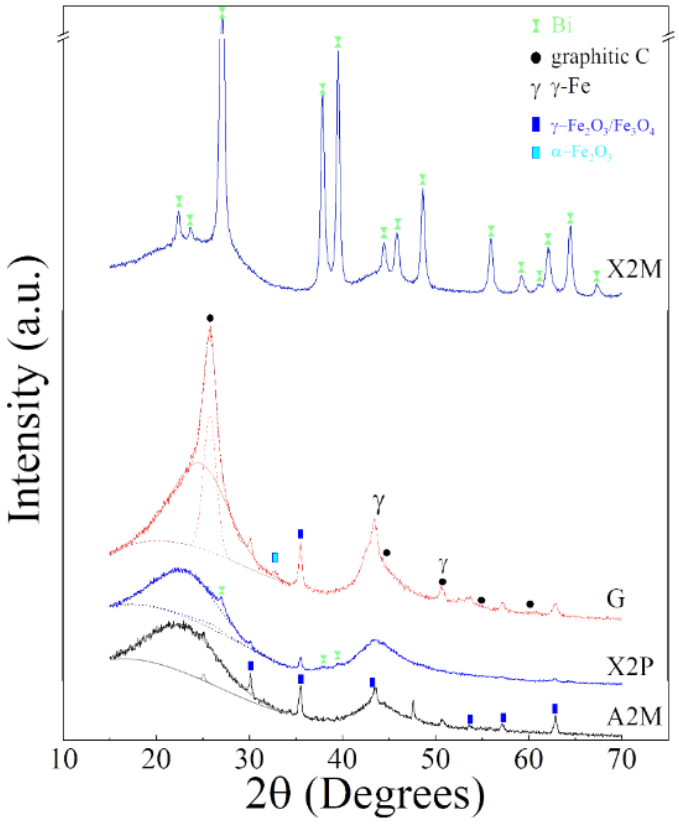

Figure 7-1. XRD diffraction patterns recorded for the CBiFe nanocomposites with different aerogel and xerogel particularities

Table 7-2. Parameters extracted from the N2 adsorption measurements using the BET, BJH and HK models

Sample	S_{BET} (m^2/g)	V_{meso} [cm^3/g]	V_{micro} [cm^3/g]
X2M	50	0.05	0.02
X2P	456	0.04	0.16
A2M	804	2.80	0.3
G	489	0.41	0.2

The xerogel sample X2P reveals a Type I adsorption isotherm (microporous materials) and a very poor H4 hysteresis (slit shaped pores in mesoporous systems). Sample X2M exhibits lower microporosity than X2P, having similar features as the CXBiFe xerogel monoliths investigated in the previous chapter. On the other hand, samples G and A2M indicate Type IV isotherms and an intermediate hysteretic behavior between H3 and H1, all signs of a well-defined porous network with higher microporous and mesoporous contributions (see **Table 7-2**).

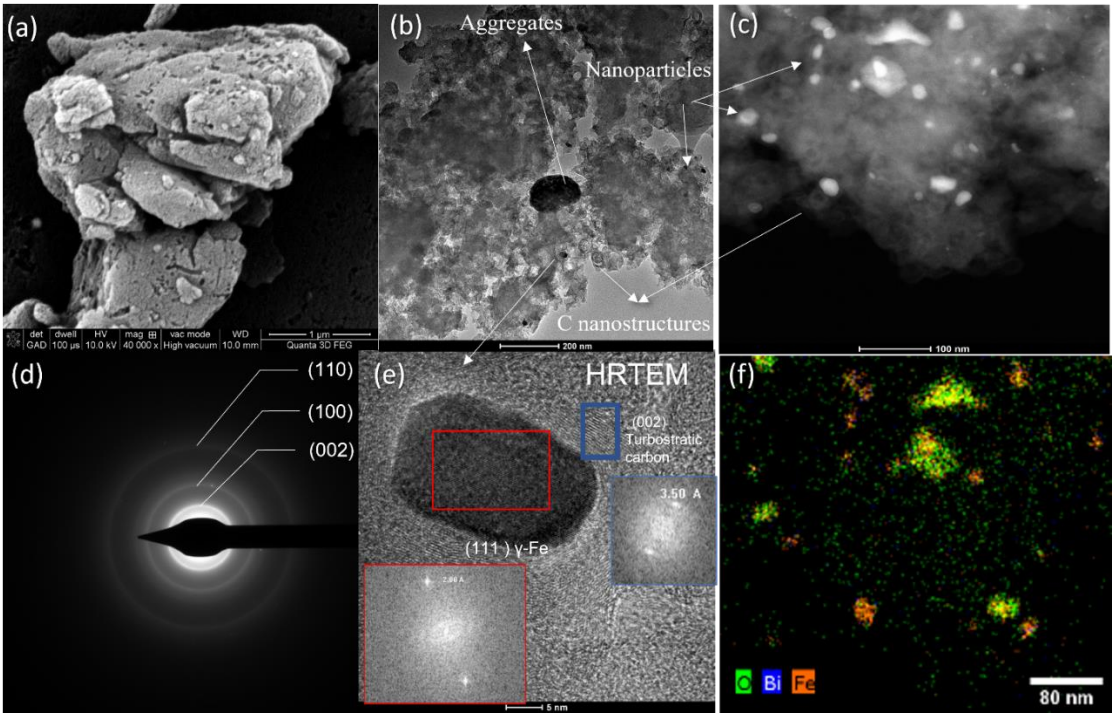

Figure 7-2. Nanoscale analysis of graphitized regions found in sample G: (a) SEM micrograph, (b) BF-TEM micrograph, (c) STEM image, (d) SAED pattern, (e) HRTEM of Fe nanoparticle surrounded by graphitized shell and (e) STEM-EDX map obtained for the region found in (c).

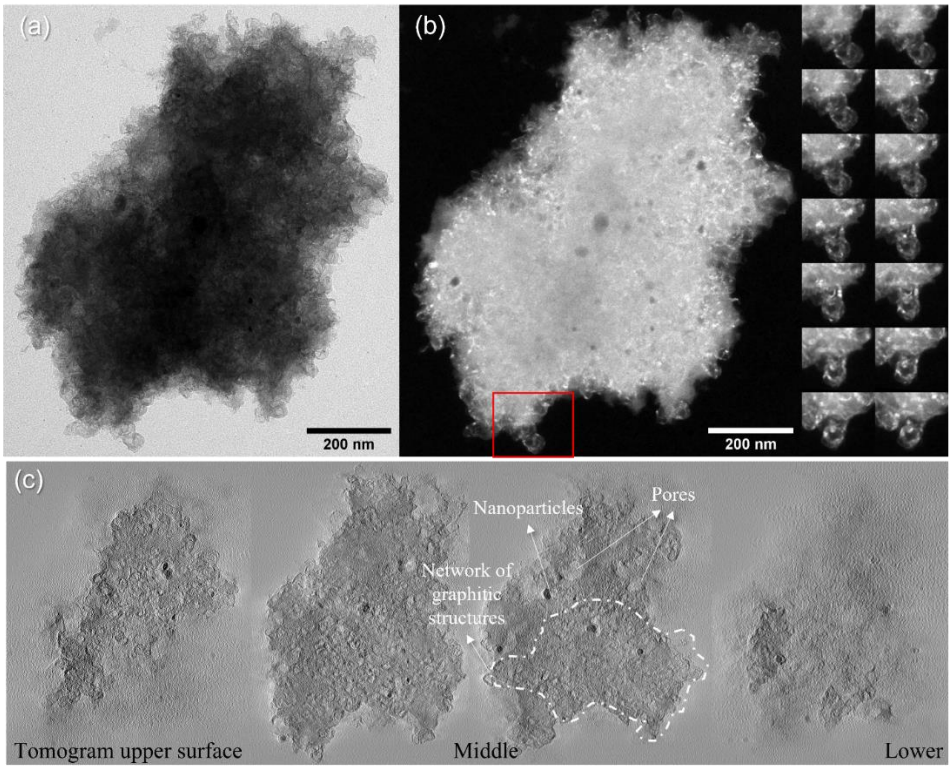

Figure 7-3. The morphology of graphitized CBiFe grains: (a) BF micrograph, (b) CDF micrograph at different α tilt angles, (c) Slices of the 3D reconstruction of the BF tilt sequence.

7.3 Advanced characterizations on the graphitized sample

In **Figure 7-2a-c**, one can compare CBiFe aggregate grains from sample G that were observed at similar magnifications but using SEM, TEM and HAADF-STEM, respectively. The presence of a clear (002) diffraction ring found in the SAED patterns (**Figure 7-2d**) indicates the presence of graphitized nanostructures across the CBiFe grain aggregates. The graphitic tubes or shells exhibit wall thickness of 6 ± 3 nm and external diameters of 37 ± 12 nm, close to the main contribution in pore diameters found during the previous SEM analysis. The HR-TEM investigations of the carbon nanostructures (**Figure 7-2e)** indicate interplanar distances between 3.4 and 3.6 Å, corresponding to the (002) plane in turbostratic and defected graphitic carbons. The nanoparticle surrounded by the graphitized shell exposed crystalline planes with an average interplanar distance of 2.09 Å, corresponding to the (111) plane of γ-Fe structure. The chemical maps presented in **Figure 7-2f** depict the spatial distribution of C, O, Fe, Bi elements. While Bi is highly diluted in the system, Fe and O elements overlap differently with the nanoparticles, suggesting the dual presence of Fe and Fe_2O_3 nanoparticles.

CDF and BF at different tilt angles were then recorded. During tilt, the brightest regions from the CDF micrographs indicate the graphitic structures. The angle dependent variations in intensity suggest that the carbon shells and nanofibers have a conical symmetry. The nanofibers are relatively short and exhibit a tortuous path that complicates their characterization. Through 3D reconstruction, we were able to evidence the catalyst activity within the CBiFe grain, together with amorphous carbon, nanoparticles and non-graphitized pores (**Figure 7-3**) and to identify carbon nanofibers with lengths of ~120 nm.[8]

7.4 Conclusions

Sample G is described as a nanocomposite based on an amorphous carbon support inside which a dense and complex branched mesopore network with both un-graphitized and graphitized pores developed via the heterogeneous graphitization. The length of the graphitic pores is estimated somewhere in the range of 20-120 nm, with an average diameter of ~40 nm and a graphitic wall thickness of ~5 nm. The average distance between the graphitic structures was observed to vary among the aggregate grains from distances comparable with the graphitic structures to larger values. According to percolation models of composite materials, an insulator to metal transition takes place when the dispersed mass of the electrically conductive filler reaches a critical value referred as percolation threshold.[49] In the case of CNT/polymer composites, Li et al. observed that the percolation threshold value for a CNT/epoxy admixture depended on three variables: (1) the *CNT aspect ratio*, (2) *disentanglement* of CNT agglomerates at the nanoscale, (3) *uniform distribution at microscale*.[50] Also, while studying random networks of SWCNTs in a thin film transistor geometry, Snow et al. addressed the percolation threshold as the CNT density at which the average distance between the nanotubes equals their average length and that the properties of the network can be treated as uniform *if the dimension of the system is much larger than average distance between the nanotubes.*[51] The overall investigations suggest that a percolation threshold might not be reached, macroscopically, most probably due to the inherent porosity, low aspect ratio and complex entanglement.[50]

8. *In situ* TEM heating experiment on RF-BiFe xerogels

8.2 Thermal stages of CBiFe nanocomposites evidenced through TG/DTG and in situ TEM experiments

Temperature program selection

The nanocomposite system obtained by following the route specific to the previousy investigated sample CXBiFe3 (1.2 mg Bi precursors, 1.2 mg Fe precursor) was selected for further pyrolysis experiments. The untreated sample will be further denoted as "OX". A TG/DTG/DTA analysis was initially performed in order to plan the in situ TEM heating and pyrolysis experiments.

The TG/DTG/DTA curves recorded between room temperature and 1100 °C (**Figure 8-1a**) outline four main temperature regimes: The sample evidences a ~25% weight loss during in the thermal range of **(20, 250 °C)**, during which several DTG maxima and endothermal DTA processes are evidenced at ~ 100, 170 and 200 °C. The most significant weight loss (~30%) is experienced on the 250-600 °C temperature interval and continued by a 10% loss between 600 and 900 °C. The DTA data exhibit a wide exothermal signal on the entire domain, probably associated with pyrolysis and combustion effects. On the final thermal interval, the sample tends to lose 20% of its mass, at increased rates with DTG maxima close to 910 and 1015 °C. The DTA curve exhibits very small variations at 884, 950 and 1035 °C, but due to the wide background/exothermal signal, their precise nature is uncertain.

Based on these results, the thermal program for the in situ TEM heating experiment (performed during the Research Internship at Ecole Polytechnique) was chosen as depicted in **Figure 8-1b**. The isothermal conditions were maintained for 15-30 min to further protect the grid from any thermal shock and to facilitate the time for investigating several regions of interest. After high temperature stabilization, faster rates were used (50 °C/min above 600 °C) to decrease the total experiment time. Video sequences were recorded during the thermal dwells at 750, 800 and 900 °C, when most of the system dynamics was observed. The 800 to 900 °C transition was also recorded, during which most important graphitization events will be observed. The representative TEM micrographs and the measured particle size distributions recorded for the main region of interest are presented in **Figure 8-1c-h**.

The cumulated TG/DTA and in situ TEM data resolve towards a 4 stage classification of the CBiFe based pyrolysis products obtained during: (1) incipient decomposition stage (100-250 °C), (2) primary carbonization (250-750 °C), (3) reduction/incipient graphitization stage (600-800 °C), followed by (4) advanced graphitization stage (800-900 °C). The description of each stage in terms of thermal processes and nanoparticle features is detailed elsewhere**.**[8]

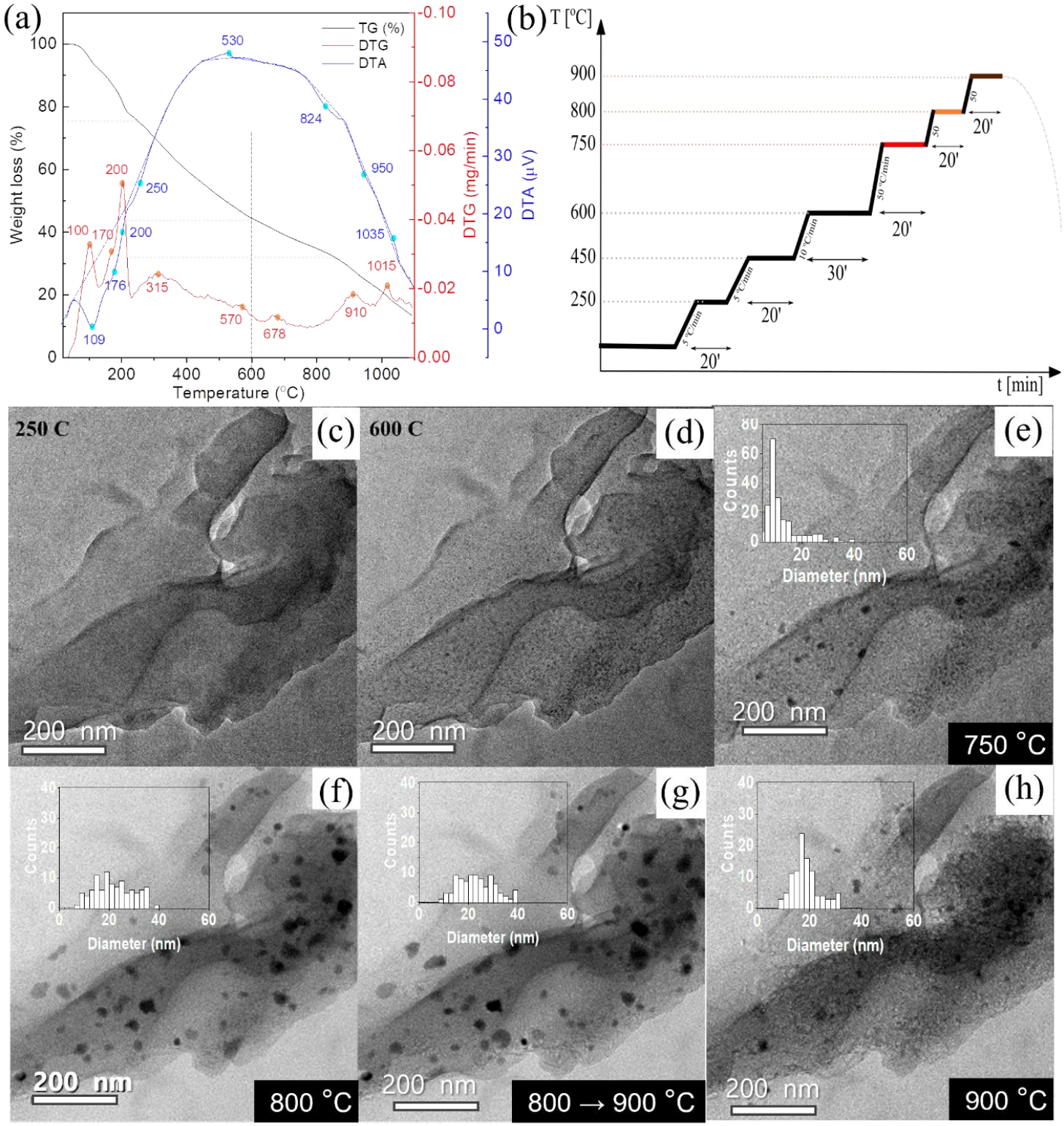

Figure 8-1. Thermal investigations of OX sample: (a) TG/DTG-DTA curves measured under N_2 flow, (b) thermal program chosen for the in situ TEM heating, and in situ BF-TEM micrograph sequences and nanoparticle size distributions grown in C-Bi-Fe aggregate at (c) 250 °C, (d) 600 °C, (e) 750 °C, (f) 800 °C, (g) during transition from 800 to 900°C and (h) during the dwell time at 900 °C after the maximum activity is observed.

8.3 Particle dynamics during in situ TEM and the graphitization mechanism

The graphitization mechanism

The system dynamics observed in the entire video footage is analyzed using image processing tools to extract any temperature dependent data related with nanoparticle movement and growth. This was obtained using a particle tracking plugin in FIJI software.[52] Nanoparticle motion relative to the carbon support was analyzed in terms of relative displacement of detected nanoparticles and mean and maximum velocities during each video sequence. Before initiating the particle tracking algorithm, the video sequences were processed so that discrimination of the moving nanoparticles would be achieved relative to the carbon support and particles at rest.

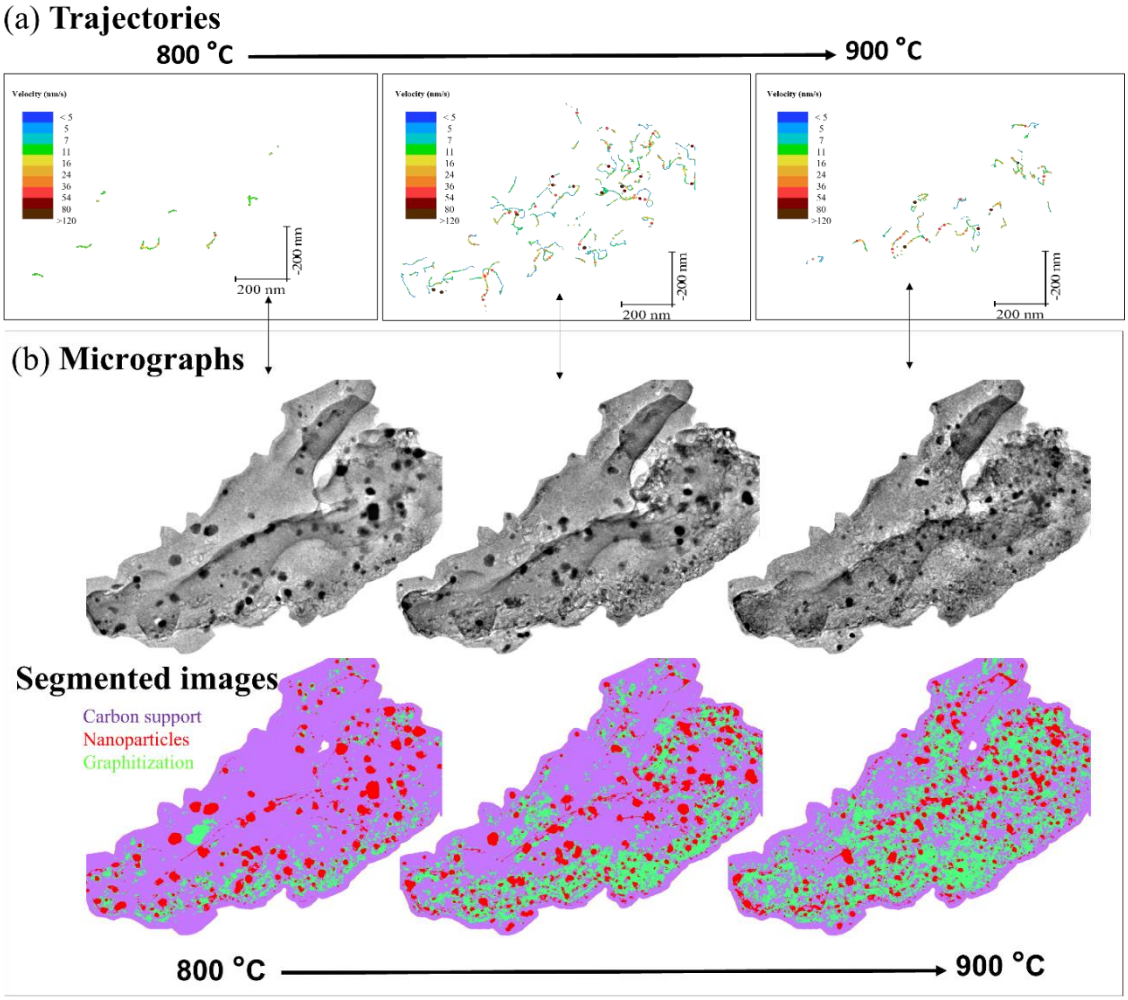

Figure 8-2. Relation between nanoparticle movement and graphitization induced texturing: (a) nanoparticle trajectories with apparent velocities (color values) and (b) textural changes observed in BF TEM micrographs and their segmented versions

The results were further expressed as distributions of the xy-projected velocities versus temperature and label of detected particle ("trajectory index") in **Figure 8-5a**. One can observe a peak describing the maximal activity somewhere between 800 and 900 °C. The average nanoparticle velocity increased with temperature from an average of 16 nm/s at 750 °C to 54 nm/s, obtained during the transit from 800 to 900 °C, and further decreased towards stationary conditions

at 900 °C **Figure 8-5b**. The growth rate of CVD grown nanotubes is generally described as an exponential dependence on temperature:

$$\gamma = B\, e^{-\frac{E_a}{k_B T}}, \qquad (8.1)$$

where γ represents the growth rate, T is the absolute temperature, k_B = the Boltzmann constant, E_a is the activation energy and B corresponds to a proportionality coefficient. The activation energy for the nanotube growth inside CBiFe was determined by fitting ln(γ) against $1/(k_BT)$ (**Figure 8-5c**). The activation energy found at lower temperatures was E_a = 0.68 eV, associated with the surface diffusion of carbon as rate limiting process.[69,138] During the enhanced graphitization stage (the increase between 800 and 900 °C), lower values of E_a = 0.29-0.34 eV were obtained. This suggests some limitations due to slower mass diffusion and carbon adsorption processes.[69,138]

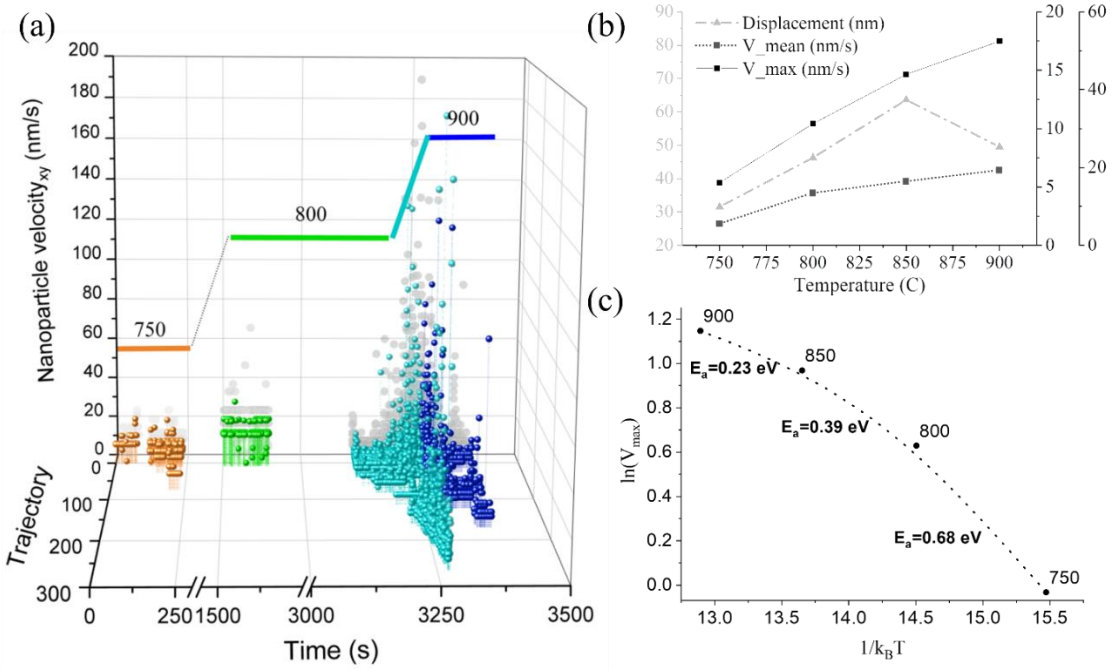

Figure 8-3. Nanoparticle dynamics during in situ TEM: (a) velocity measured for moving nanoparticle versus time and trajectory index (b) estimated displacement (nm), mean and maximum velocities averaged across the entire set of nanoparticles versus temperature and (c) apparent activation energies determined using the exponential model for nanotube growth

8.4 Conclusions

During the in situ TEM investigations of graphitization inside a CBiFe system, the nanoparticles show a limited amount of displacement (50-100 nm) before repose. Considering the details found when analyzing the adsorption/diffusion processes of carbon sources, we associate these effects with lower available gaseous feedstock concentrations. As opposed to the typical CVD set-ups, where the partial pressure of the carbon source is fairly constant, the thermal evolution of species such as CH_4 and CO decrease with the progress of the thermal treatment after 600 °C. In conclusion, we assume that an increase in CO (and CH_4) partial pressure may add several benefits: the carbothermal reduction and catalyst activation would increase along with the overall nanotube lengths and graphitization yields.

9. Pyrolysis related effects over the nano-scale: nanostructures found in CBiFe xerogels

Table 9-1 Sample notation and parameters used during the pyrolysis of CXBiFe nanocomposites

	Sample	Xerogel State	Pretreatment (*)	Temp [°C]	Dwell time [h]
Samples treated at high temperatures under N_2					
	N750_1M	Monoliths	N_2, 250 °C, 2 h	750	1
	N900_5M		N_2, 250 °C, 2 h	900	5
	N1050_1M		N_2, 250 °C, 2 h	1050	1
	N750_1M2 (**)		N_2, 450 °C, 2 h	750	1
Samples treated at high temperatures under Ar (95%) - H_2 (5%) (**)					
	NAH750_1M	Monoliths	N_2, 450 °C, 2 h	600	1
	NAH600_1M			750	
	NAH900_1M			900	
	NAH750_1P	Powders		600	
	NAH600_1P			750	
	NAH900_1P			900	
Samples treated at high temperatures under Ar					
	A600_2M	Monoliths	Ar, 250 °C, 2 h	600	2
	A750_2M			750	
	A900_2M			900	
	A1050_2M			1050	
	A1050_2M2		No	1050	
	A1050_2p2	Powders	No	1050	

(*)The same temperature increase rate (3°C/min) was used for all the considered thermal programs. (**)The NAH and N750_1M, N750_1p samples were pyrolyzed in a second quartz tube furnace (PMC Laboratories at Ecole Polytechnique, France), while the pyrolysis under Ar and N_2 were made using the original quartz tube furnace as for previous chapters.

Figure 9-1 CXBiFe monoliths after pyrolysis under (a) Ar, (b) N_2 and (c) N_2 / Ar+H_2 at various temperatures

9.1 Introduction

To complement the previous in-situ TEM and TG-DTA investigations with structural and compositional data, the pyrolysis induced changes taking place in CBiFe nanocomposites at the

nano-scale are investigated. The particularities of each thermal program considered during the following two chapters are summarized in **Table 9-1**.

The samples after pyrolysis are shown in **Figure 9-1**. As before, the monoliths obtained during the pyrolysis experiments under N_2 and Ar exhibit a metal/oxide surface crust colored from iridescent-blue (mostly attributed to Bi deposits) to rusty orange (attributed to Fe_2O_3 aggregates) **Figure 9-1a**. On the other hand, as shown in **Figure 9-1c**, the absence of oxidic crusts in the NAH and N750_1M2 samples indicate superior reduction conditions. As before, the samples were investigated using XRD, TEM, SEM and Raman. Graphitizatized nanostructures were evidenced only in the Ar treated sample batch, specifically for A1050_2M sample. For this reason, more in depth morphological and structural analysis as well as electrochemical investigations were performed for this set of samples. The main results are outlined in the following.

9.2 The Bi and Fe based phases at the nano-scale

Pyrolysis experiments under Ar

Starting with the samples treated under Ar atmosphere, the XRD patterns evidence the crystalline phase changes with temperature for different pyrolysis conditions, as shown in **Figure 9-2**. The A600_2M and A750_2M samples show crystalline β-Bi_2O_3 forms together with γ-Fe_2O_3. Near the strongest β-Bi_2O_3 peak, an additional amorphous peak is maintained around $2\theta = 28°$ for samples treated below 1050 °C. The main β-Bi_2O_3 peaks found for the A750_2M sample are smaller relative to the 28° amorphous hallo. This may represent mainly signs of Bi-O-Fe interactions that may compete with the crystallization process.[9] Metallic bismuth, and iron are the dominant crystalline phases for the A900_2M and A1050_2M samples. Finally, bismuth reflections decrease after pyrolysis at 1050 °C, due to smelting and long dwell times. The γ-Fe_2O_3/Fe_3O_4 signals are better defined simultaneously with γ-Fe. No clear contributions of the (002) reflection for turbostratic carbons are evidenced, which contrasts with the in-situ TEM findings presented in the earlier chapter.

Transmission electron microscopy

The TEM investigations support that the dominant traits observed for all investigated xerogel samples are specific to a carbonization/reduction stage. The complex dumbbell structures that were evidenced in **Chapter 6** in the CXBiFe composite treated at 750 °C under N_2 purge were also observed in the present samples at different temperatures and types of atmospheres. Having in mind the smaller bulk melting temperatures of Bi and Bi_2O_3 (T_{Bi} = 271 °C K and T_{Bi2O3}= 817 °C) with respect to iron and iron oxides (T_{Fe} = 1538 °C and $T_{Fe2O3\text{-}Fe3O4}$ ~ 1567-1597 °C), the Bi phase will diffuse more efficiently onto the carbon surface, while Fe_2O_3 clusters may serve as anchoring sites and further result in BFO structures, strongly dependent on the local conditions.[9] A STEM/EDX analysis was performed on the samples treated at 750 and 1050 °C under N_2 purge, as summarized in **Figure 9-3**. At low magnifications, one can observe that the occurrence of hybrid BFO structures is higher for the sample treated at 750 °C. Instead, for the 1050 °C treated sample, nanoparticles with more homogeneous composition of Fe (or Bi) start being observed with a higher frequency. The STEM-EDX maps showing the distribution of Bi, and Fe elements also support this trend.

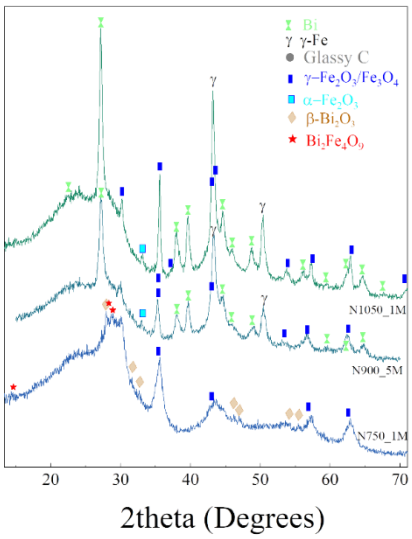

Figure 9-2. XRD patterns recorded for samples treated under Ar flow at different temperatures

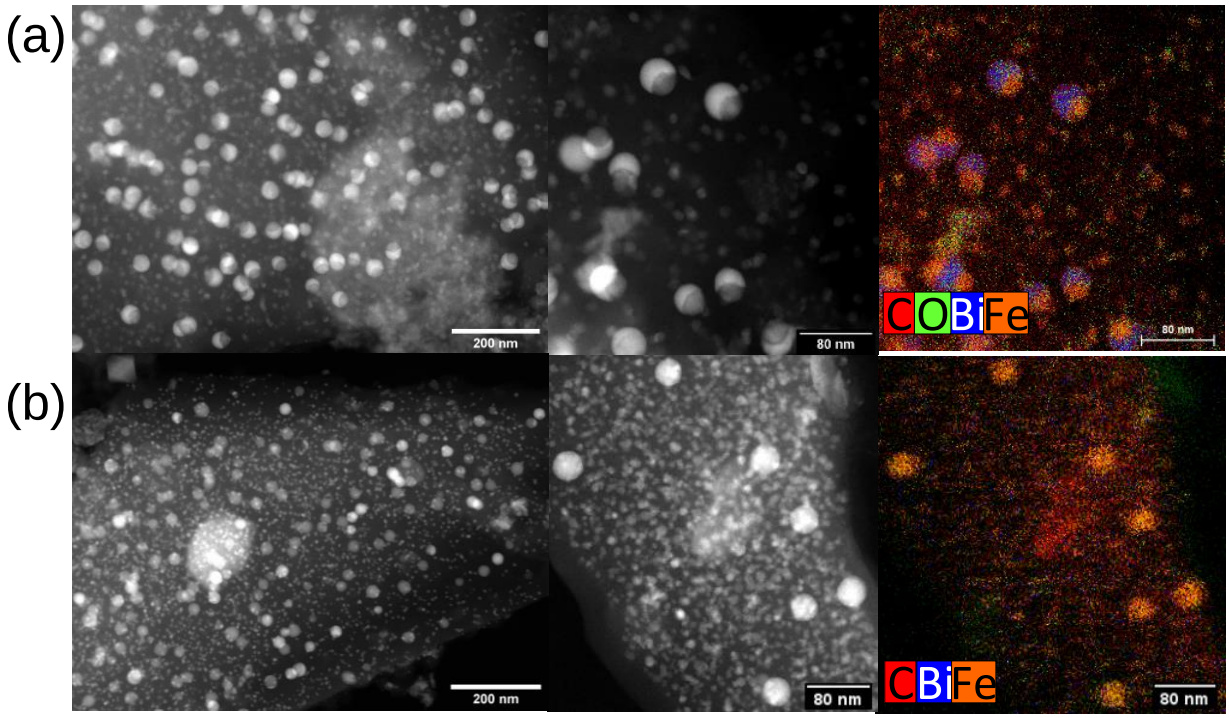

Figure 9-3. STEM-HAADF micrographs and STEM-EDX maps obtained on samples treated under N_2 at (a) 750 °C and (b) 1050 °C.

9.3 Carbon at nano-scales

TEM investigations

Under STEM mode, the BSUs were discriminated for samples A600_2M and A900_2M (**Figure 9-4**). Two iFFT filters are also applied to the micrographs to reduce noise and to better distinguish the features.[55] It is thus revealed that the present xerogel carbon supports consist in a network of small carbon pebbles with sizes smaller than 2 nm with micro- and meso- pores forming in the inter-particle space. The structural evolution of the carbon support was characterized using

the SAED patterns for shown in **Figure 9-5** indicate predominantly amorphous features found for both samples treated at 600 °C, where no clear diffraction rings were observed for carbon, to well defined diffraction rings for treatments above 700 °C that correspond well with the ~2.0 Å and ~1.2 Å interplanar distances and are ascribed to the (100)/(101) and (110)/(112) planes formed within the BSUs of the xerogels and in other carbon structures.[56] This may correlate with the transition from the insulating to conducting state observed by others.[57] For sample A1050_2M (right side in **Figure 9-10b**), where graphitized regions were also discovered, the SAED patterns from such regions include an intense ring (~3.4 Å) and a lower intensity ring (~1.2 Å) specific to diffraction from the (002) and (004) planes found in graphitic nanocrystals.[56]

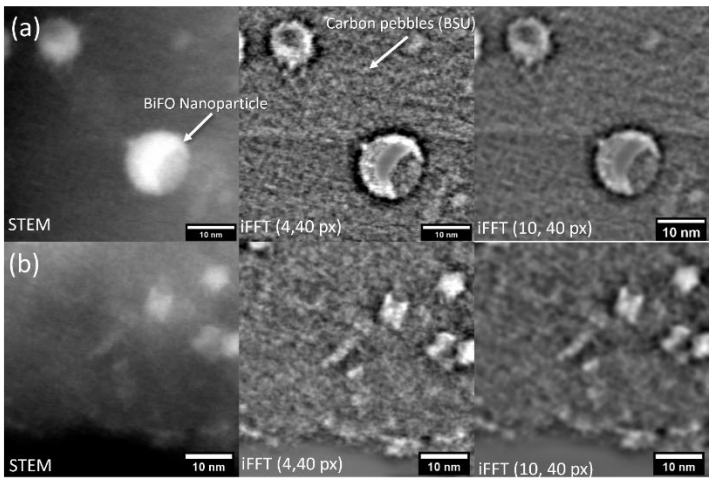

Figure 9-4. STEM-HAADF analysis of samples (a) A600_2M and (b) A900_2M revealing the basic structural units (BSU) as small C pebbles forming the carbon support

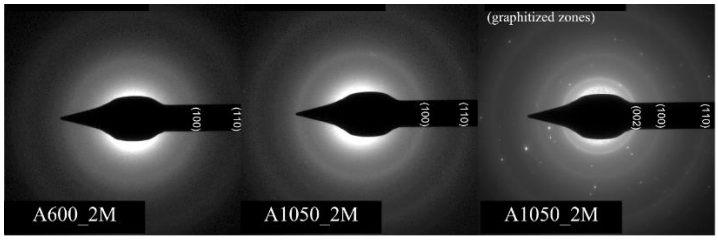

Figure 9-5. The effect of pyrolysis temperature over the crystallinity of the carbon support as seen in the SAED patterns for CXBiFe nanocomposites treated under (a) N_2 / Ar+5% H_2 and (b) Ar purge

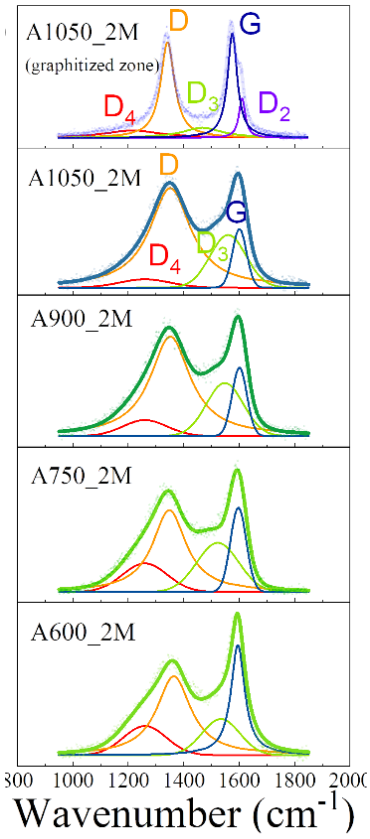

Figure 9-6. Raman spectra of CXBiFe nanocomposites treated at various temperatures under Ar purge

Raman analysis

Further on, we focus on the typical Raman spectra recorded for samples treated under Ar purge at different temperatures as shown in **Figure 9-6.** By comparing the Raman spectra obtained at various temperatures, the untreated samples and those treated at 600°C exhibited a background with a positive slope. while at higher temperatures, a relatively constant background was observed. This effect is probably correlated with photoluminescence quenching process and reduction of CH treatments applied at higher temperatures.[58] Further on, background subtraction was performed

before analysis of the first order and second order regions. Following the D and G Raman bands (**Figure 9-12b**) in both types of pyrolysis experiments, one can observe that with the increase in temperature, the I_D/I_G ratio is also observed to gradually increase. The 4 peak fit results are overlapped with the raw spectra and the G position and FWHM are presented for all samples analyzed using Raman spectroscopy in **Figure 9-7.** A blue shift and a decrease in FWHM trends were additionally remarked for the G peak with the increase in pyrolysis temperature. The same spectral changes were observed while probing the nanocomposites treated under Ar purge with a 785 nm excitation line. Considering the amorphization/ordering trajectories proposed by Ferrari et al,[59] these trends correlate with a temperature induced increase in short range order for sp^2 rich nano-crystalline carbons, consistent with the STEM observations of small BSUs the temperature evolution of the SAED patterns. The regions with higher graphitization yields induced by the catalytic activity of Fe nanoparticles, which were exclusively observed in the A1050_2M sample (**Figure 9-12b**-top), gave rise to Raman spectra with significantly narrower D and G bands centered at 1341 and 1575, respectively, with no significant D_4 and D_3 contributions. Due to the shift of the G signal, the D_2 band was evidenced as a shoulder and included as separate contribution during the fitting process. These features are specific to a superior, graphite like crystallinity that is also found in other structures such as carbon nanotubes and nano-fibers. In the region of second order harmonics (2500 – 3500 cm^{-1}), the cumulative intensity is observed to decrease with pyrolysis temperature relative to the intensities of the first order region. The graphitized regions from A1050_1M reveal a highly amplified 2D band which also confirms an increased level of organization.

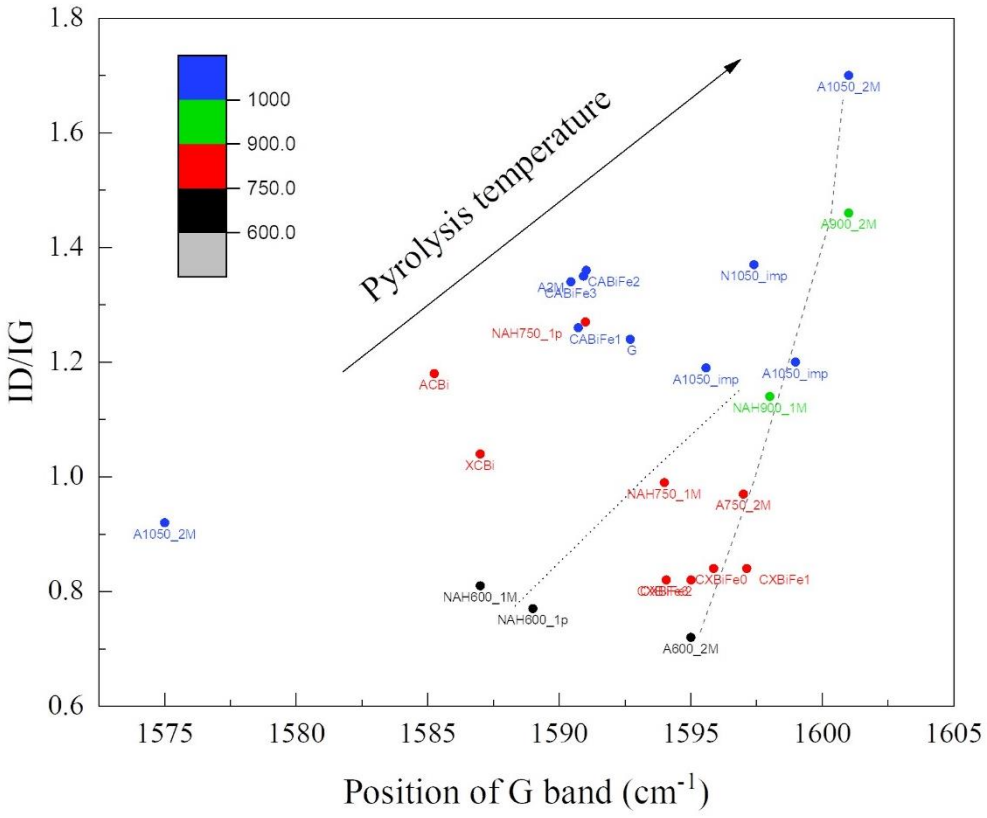

Figure 9-7. Overall Raman results expressed as I_D/I_G versus G band position obtained after performing the 4 peak fit procedure for various CBi and CBiFe xerogel and aerogel systems.

9.4 Conclusions

Overall, the correlated XRD, TEM and in situ TEM results suggest that, for the pyrolyzed samples, a delay is experienced when compared to the dynamics observed during the in-situ TEM experiment. The results support that during the reduction stage, i.e., when the melting temperatures of Bi_2O_3[60] or the peritectic decomposition of $Bi_2Fe_4O_9$[61] is reached (T_{Bi2O3} ~ 824 °C and T_{BFO} ~ 825-937 °C, respectively), the hybrid nanoparticles may separate at the interface between Bi and Fe rich regions. Thus, it is plausible that Fe catalysts that support the heterogeneous graphitization, may not be active until this separation takes place. As observed in the earlier chapter, during the high-vacuum in-situ TEM experiment, multiple nanoparticle splits were observed starting from 750 °C, when the first graphitization phenomena were also observed. The 5-10 nm nanoparticles were largely absent at 800 °C and the graphitization activity was highest during the transition from 800 to 900 °C. The dissimilarities observed between the present samples and the in-situ TEM experiment can be explained due to the significantly longer treatments and a more oxidized environment. The results of the pyrolysis experiments support that the absence of a strong graphitic contribution to the X-ray diffractograms mainly due to bismuth and oxygen impurities that hinder the catalytic role of Fe NPs, followed by low carbon feedstock availability as pyrolytic gases.

10. Pyrolysis related effects over the porosity and micro-scale of CBiFe nanocomposites

10.1 Introduction

Following the broad results obtained on the previous chapters, the present chapter further refines the analysis of the Ar treated samples that were introduced during the **Chapter 9** (samples A600_2M, A750_2M, A900_2M and A1050_2M). The purpose is to obtain information about the influence of the pyrolysis on the nanocomposite at larger scales in terms of: (1) the spatial distribution of the different phases encountered in CXBiFe nanocomposite monoliths, (2) the micro- and meso-porosity and (3) aggregate size evolution during grinding.

First, the monolithic structures are investigated using macro-photography and SEM/EDX at meso- and micro-scales. The SEM analysis of each sample basically consisted in a panoramic view of the CBiFe cross-sections at low magnifications for identification of regions of interest (50x), an EDX analysis of different regions of interest at intermediate magnifications (200-400x) and feature discrimination at high magnifications (5000-30000x). The nanoparticle distribution within the carbon support that forms the monolithic core is addressed using SEM and advanced image processing techniques (image filtering, segmentation and Voronoi tessellation). The quest for graphitized carbon structures introduced during the previous two chapters is supplemented with a final SEM/Raman investigation of the A1050_2M after sample fracturing and rough polishing. Details regarding the porosity of the samples treated at various temperatures under Ar purge are obtained using the N_2 sorption porosimetry. Finally, since different temperatures are expected to change the mechanical properties, thus influencing the CXBiFe aggregate grain size during mechanical grinding (performed under the same conditions: grinding at 25 Hz for 2 min), the SEM investigations performed on the ground samples is complemented with diffuse light scattering analysis (DLS) for determining the size distribution of aggregates smaller than 6 μm. Along with the nano-scale effects observed in the previous chapter, the three mentioned aspects, nanoparticle

size distribution, porosity and aggregate size distribution are expected to play significant roles in the analytic applications described in the final chapter. In the context of electrochemical studies, the nanoparticle size histograms (NPSH) and intra-particle distancing, ascribed through tessellation and Voronoi domain size histograms (VDSH) are considered as highly relevant in describing the microscopic coverage of electrochemically active metal/oxide centers during voltammetry experiments at heterogeneous electrodes.[62] The porosity and aggregate size distribution will impact the electronic transport properties and the macroscopic surface coverage respectively.

10.2 The spatial distribution of Bi/Fe nanoparticles

Macro-photography and low magnification SEM/EDX

The panoramic views obtained by stitching SEM micrographs of the monolith cross-section are presented in **Figure 10-1**. The micrographs well emphasize the presence of microscopic pores cavities and cracks. The oxide rich layers that form the metal-oxide crust are observed in the vicinity of the lateral surface. The EDX derived composition from the core is based on C as the primary element (over 90 at%), followed by O (3-7 at%), Fe (0.2-1.3 at%) and Bi (below 0.8 at%). A trend of decrease in Bi contributions is observed with the increase in temperature, which is consistent with the previous XRD studies.

The core of the monolith is based on aggregate structures with a glassy-smooth appearance. Bismuth based micro-needle structures were observed more frequently in the samples pyrolyzed at lower temperatures and are considered the main pathway for bismuth losses. At larger magnifications, the CBiFe aggregate grains reveal the presence of nanoparticles embedded into the carbon support. It is necessary to note here again, that this feature is the most dominant in CBiFe nanocomposites, considering their high occurrence frequency during TEM and SEM investigations.

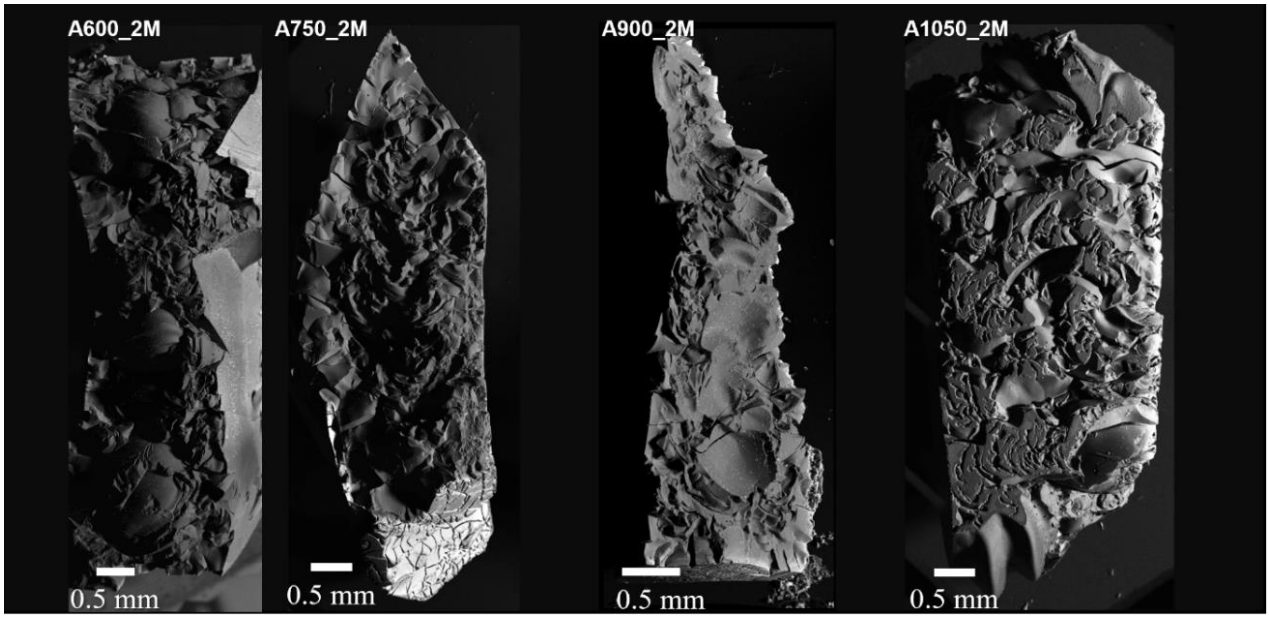

Figure 10-1. Meso-scale analysis of fractured CBiFe monoliths: panoramic view obtained by stitching SEM micrographs (50x). The A1050_2M sample was polished before the microscopic analysis.

Nanoparticle size histograms (NPSH) Voronoi domain size histograms (VDSH)

To derive NPSHs and VDSHs from SEM analysis at large magnifications, the core regions from powdered monoliths were primarily investigated. SEM micrographs were acquired at magnifications of 24000-80000x. The results of the SEM analysis on the CBiFe samples treated under Ar flow at different temperatures are presented in **Figure 10-2.** From the presented SEM micrographs and the obtained NPSH and VDSH plots, one can observe an increase both in size and intra-particle distance, with pyrolysis temperature, at the expense of lower nanoparticle population densities. Even though the given measurements are still affected by noise and resolution, the trend is maintained at multiple scales.

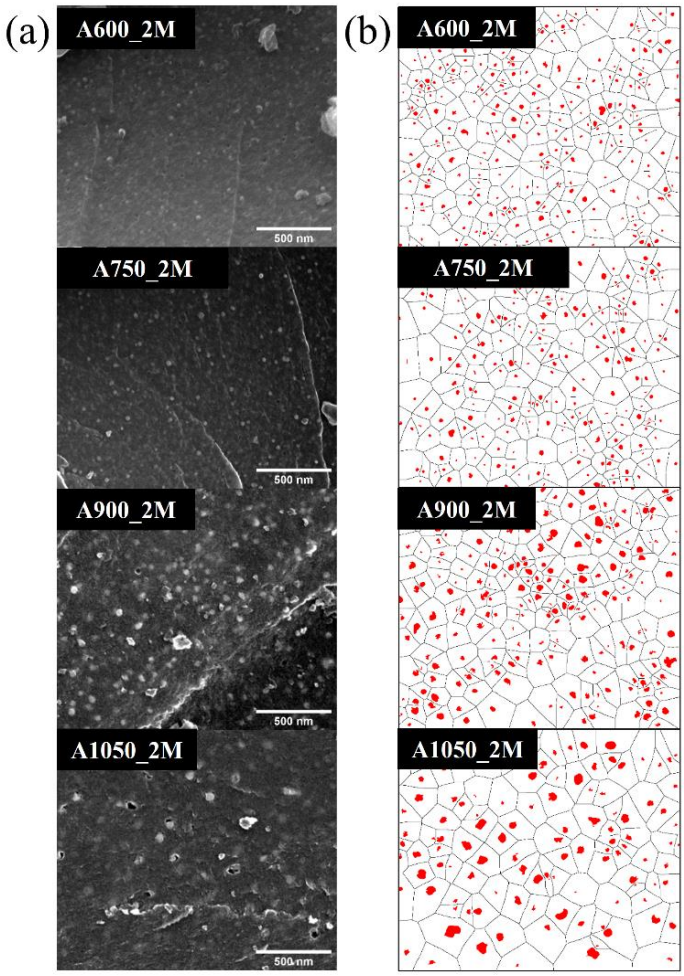

Figure 10-2 –SEM analysis of Ar treated samples for nanoparticle distributions: **(a)** SEM micrographs at 80 000 x of an aggregate grain exposed through grinding, **(b)** results of the image processing sequence for particle detection and Voronoi tessellation for the same micrographs

Table 10-1. Average nanoparticle diameter (D_{np}), Voronoi domain diameter (D_{VD}) and microscopic coverage (θ) for various CBiFe nanocomposite xerogel and aerogel samples

Sample	Temp. [°C]	D_{np} [nm]	D_{VD} [nm]	θ
A600_2M	600	19	119	0.03
A750_2M	750	21	128	0.03
A900_2M	900	29	140	0.04
A1050_2M	1050	36	164	0.05
X_{Bi}_750N_2	750	30	101	0.09
A_{Bi}_750N_2	750	108	176	0.38
N750_1M	750	9	75	0.01
N1050_1M	1050	39	176	0.05

The statistical analysis of the acquired data is summarized for each sample in terms of D_{np} - average nanoparticle diameter and D_{VD} -average Voronoi domain diameter, as presented in **Table 10-1**, together with the values obtained for the samples investigated in the previous chapters. The averaged microscopic coverage of metal/oxide centers θ[63] is included as:

$$\theta = \left(\frac{D_p}{D_D}\right)^2$$

It is expected that during the pyrolysis experiments, the θ parameter will exhibit a maximum during reduction and incipient graphitization stage, followed by a decrease due to Bi losses (i.e. conditions similar with the in situ TEM). However, for the majority of the presented experiments, the inflection is delayed at higher temperatures, given the oxygen impurities that yield higher reduction and melting temperatures. The Fe based nanoparticle population may grow after BFO splitting and the size decrease may take place during enhanced reduction/graphitization stages.

10.3 The spatial distribution of carbon structures: the quest for graphitized structures using SEM/EDX and micro-Raman investigations

2D Raman profiles were acquired from different regions and scales: transverse cross-section of the core (16 points per 2080 μm), cross-section of CBiFe aggregate (100 spectra per 100 μm), Z-profile from the crust (50 points per 5 μm) and three different regions found near the crust-core interface (~1 point/μm). For analysis and interpretation, data normalization was considered. The recorded data is summarized in **Figure 10-3** as 3D plots (top view). Regarding the monolith core, the spectral data were found to consist only in the amorphous carbon specific signals analyzed in **Chapter 10**, section 10.3. This suggests a fair homogeneity of the carbon structural features found in the main CBiFe feature, the core of the monolith. The depth profile obtained from the external crust (**Figure 10-3-**right) indicates the presence of additional low intensity bands around 215, 286, 401, 480, 615 cm^{-1} that were assigned to the mixture of magnetite (Fe_3O_4) and maghemite (γ-Fe_2O_3) phases.86,147

The isolated regions found at deep core-crust interface regions (**Figure 10-4**abc) indicate the presence of graphitized carbon (**Figure 10-4bc**): one can observe that the $2D_1$ peak maxima are correlated with inter band minima between the D and G bands, both seen to have a clear spatial dependence. Considering that the distance between two adjacent laser spots is 1 μm and the probe diameter is close to 0.83 μm, an estimated size range of 2.5-5 μm is found for the graphitized regions. These values are close to the Fe nanoparticle islands formations observed in the SEM micrographs in **Figure 10-4**. Such features confirm that the catalytic graphitization process is active at 1050 °C, at least in an incipient stage in isolated regions found at the transition between the core and the crust, where iron concentrations are high, also gaseous carbon feedstock is presumed to be also high, while the oxygen levels are low enough to obtain reduced Fe catalysts.

The Raman measurements proved highly useful in discriminating different carbon phases, as well as detecting the metal oxides. The complex, non-planar shape of the samples and the long acquisition times needed for Raman maps represent the main challenges in characterizing the spatial distribution of the nano-composite phases on a larger scale.

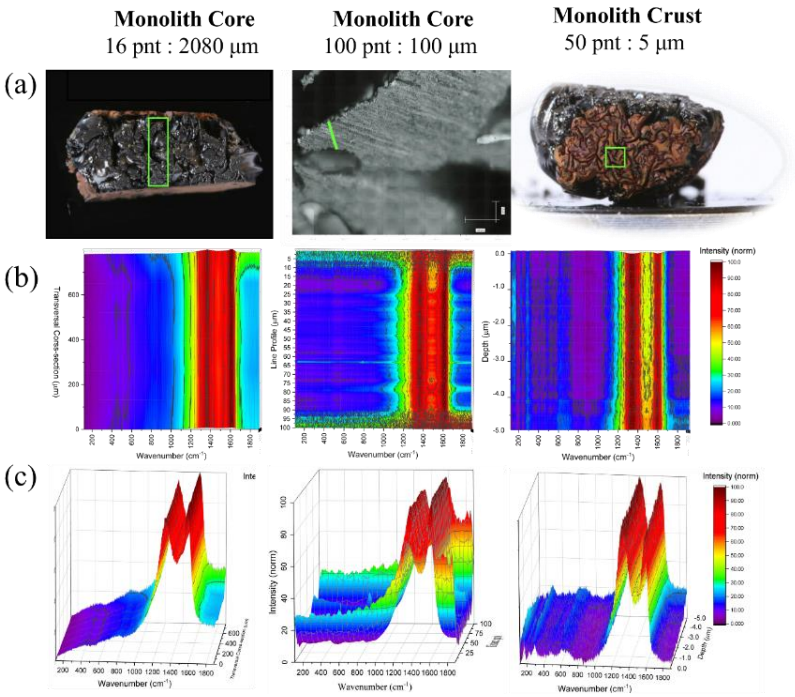

Figure 10-3. 1D Raman spectra acquired from different regions found in the A1050_2M monolith: (a) cross-section from the entire thickness of the monolith, (b) cross-section of CXBiFe aggregate grain and (b) a 5 µm depth-profile acquired from the crust of the monolith

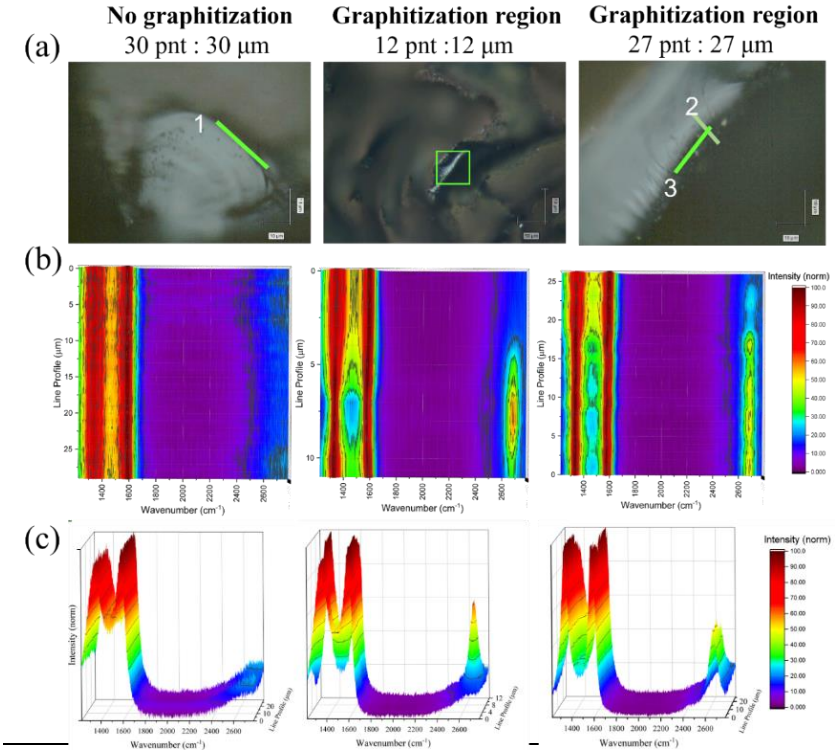

Figure 10-4. 1D Raman spectra acquired from transition regions found in the A1050_2M monolith sample: (a) region showing no graphitization – line1 and region with graphitization investigated from two different directions (b) line 2 and (c) line 3 respectively

10.4 Pore analysis through N_2 porosimetry

N_2 adsorption measurements were performed to evaluate the effect induced by the pyrolysis treatment on the mesoporous features of the composites. The results are specific to compact aggregate powders (low mesoporosity) with non-rigid slit shaped micropores, similar to pigments and activated carbon systems. The untreated xerogel sample indicates a small S_{BET}= 10 m^2/g. The thermal activation process above 600 °C favors the increase in surface area (S_{BET}= 229 m^2/g for A600_2M). The further increase in treatment temperature, indicates a gradual decrease: 146, 91 and 16 m^2/g for A750_2M, A900_2M and A1050_2M. The obtained results suggest that the pyrolysis temperature will impact the porosity of CBiFe nanocomposites through a densification process at micro-pore scales. This is confirmed by similar studies where a progressive decrease in S_{BET} and micropore volume was also observed.[41]

10.5 Effects over the size of CBiFe aggregates

Due to changes in the porosity, the mechanical properties of the CBiFe systems may also change with the applied pyrolysis conditions. This is also reflected in the aggregate size distribution after sample grinding under controlled conditions. The average size obtained from the DLS measurements for the CBiFe aggregate grains is D_{DLS}={1400, 740, 655, 570 nm} from lower to higher treatments. The SEM and DLS results thus confirm that, under controlled grinding conditions, the pyrolysis temperature will also impact the size distributions of the CBiFe powders. It is possible that this effect may contribute to changes in the global electrode surface coverage and thus, the CBiFe aggregate grain size distribution may be an important parameter when comparing the electrochemical performances of electrodes modified with different CBiFe powders, even though the nanocomposite amount is kept constant.

10.6 Conclusions

In the synthesis of CBiFe nanocomposite materials, the pyrolysis step is observed to impact several parameters at different spatial scales. As temperature and/or dwell time increase, the nano-particle growth during carbonization and reduction stage is observed, together with coalescence and mobilization of the melted Bi nanoparticles. These processes will further generate changes in the population of nanoparticles, intra-particle distancing, as confirmed by SEM-EDX and Voronoi tessellation. Further on, SEM and Raman investigations indicate that the core of the monoliths have a preponderantly homogenous distribution of vitreous carbon features, and that more oxygen defected carbon is present in the external crust. Signs of heterogeneous graphitization are observed preponderantly in the core-crust transition region, suggesting that the process might be surface sensitive, or nucleation centers may form initially towards in the transition zone of the monolith structures, where higher concentrations of catalytic Fe nanoparticles are found, together with intermediate oxygen levels, and further advance towards the core of the monolith. N_2 sorption studies further revealed that the porous features are also highly influenced by pyrolysis treatment, as densification at micro-pore scales is expected to take place. An increase in macro-porous features induced by pyrolysis temperature could not be evidenced. Lower CBiFe aggregate grain sizes are evidenced at higher treatment temperatures through SEM and DLS techniques.

11. Electrochemical tests and correlations

11.1 Introduction

The present chapter briefly summarizes the results obtained and published, for some of the previously characterized samples, using several electrochemical techniques: electrochemical impedance spectroscopy (EIS), heavy metal detection using square wave anodic voltammetry (SWAV) and hydrogen peroxide (H_2O_2) detection using amperometric measurements.[5,7,9]

The EIS investigations were performed to evaluate the effects induced by parameter variations during CBiFe synthesis and processing over the electrical (electrochemical) and interface properties of the modified electrodes. The detection of heavy metal species from aqueous environments (mainly Pb^{2+}) was performed using square wave anodic stripping voltammetry (SWASV) at concentrations near or below the limits accepted for drinkable water according to the international standards.[2] The chapter concludes with correlations found between the effects induced by the parameter variations for the material synthesis over the sensor characteristics.

11.2 Electrochemical impedance spectroscopy (EIS)

The fit results obtained for EIS investigations performed on a set of CBiFe samples are presented in **Figure 11-1bc**. The results obtained for the sample batch describing the effects of Fe concentration during the co-synthesis and Fe enrichment approach (see **Chapter 7**) indicate a negative effect over the charge transfer resistance (R_{CT}) and constant phase element (CPE). For the sample batch describing the pyrolysis effects (samples A600-1050_2M introduced in **Chapters 10-11**), both R_{CT} and CPE decrease with temperature, consistent with a decrease in porous features, as well as the insulator to conductor transition for the carbon support. Other effects such as increased reduction yields may also add to this effect. More experimental and theoretical evidence is thus required.

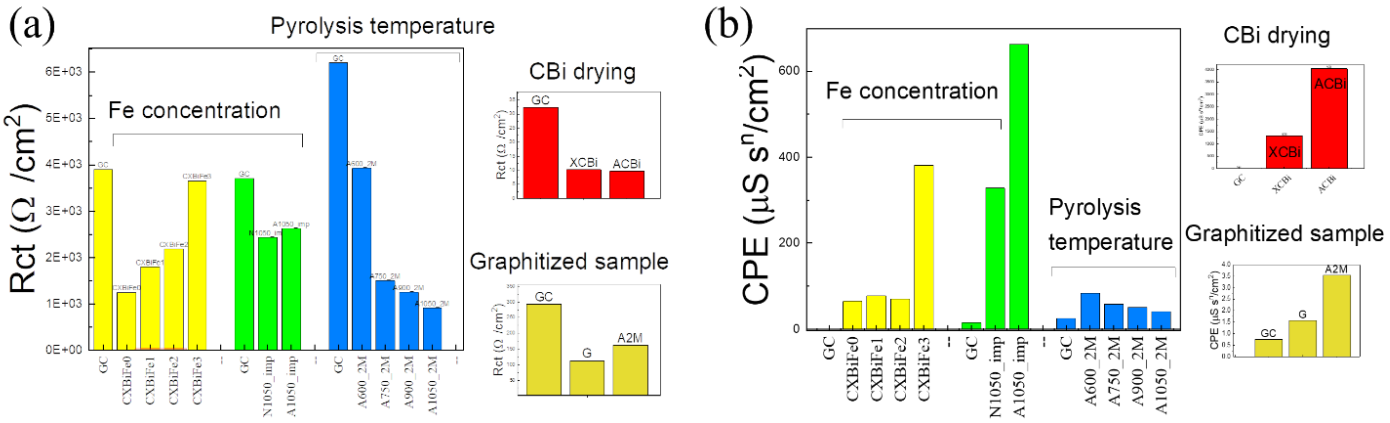

Figure 11-1. EIS investigations of CBi and CBiFe nanocomposites: (a) charge transfer resistance (R_{CT}) and (b) constant phase elements (CPE) values obtained for different CBi and CXBiFe sample batches. The values are compared with the ones obtained for the glassy carbon (GC) electrode during tests for each sample batch.

11.3 Heavy metal detection

Pb detection through square wave anodic voltammetry (SWASV)

The evaluations of heavy metal trace detection using SWASV experiments with GC-chit-CBiFe modified electrodes are summarized in **Figure 11-2**. Overall, the results indicate that most CBi and CBiFe nanocomposites can detect Pb^{2+} concentrations in trace amounts (typical range of concentrations that were tested: 1pM - 10 or 10-100 pM), thus supporting their applicability as sensor materials for heavy metals.

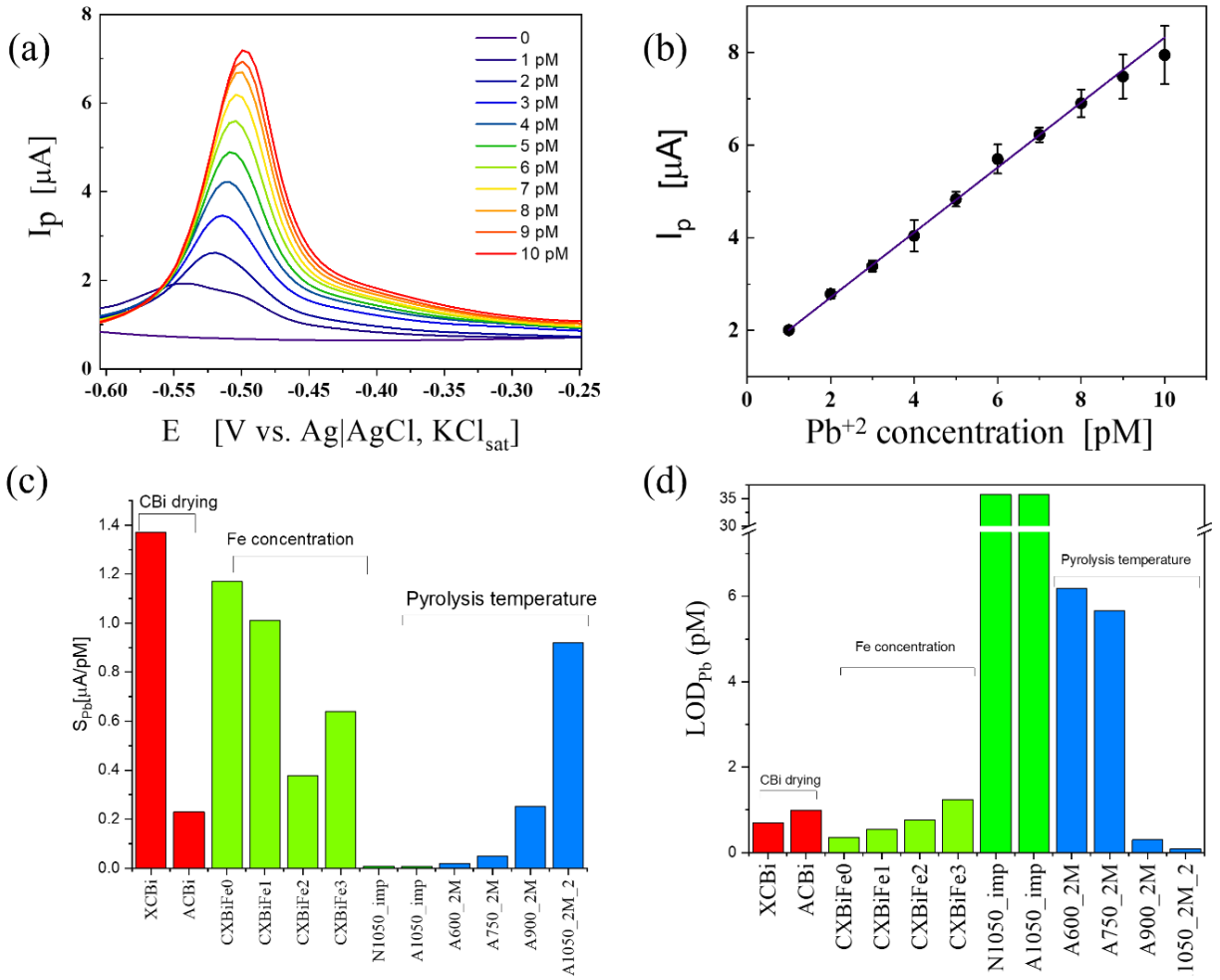

Figure 11-2. Temperature dependence for different morpho-structural and electrochemical parameters: (a) S_{Pb2+} and LOD_{Pb2+} from SWASV tests, (b) R_{CT} and CPE from EIS fit results, (c) average CBiFe aggregate size derived from DLS and the S_{BET} parameter from N_2 adsorption, (d) I_D/I_G ratio from Raman fit results and (e) average particle size ($D_{nanoparticle}$), Voronoi domain size ($D_{Voronoi}$) and microscopic coverage (θ) derived from SEM measurements

Good correlations are observed between the SWASV data and the specific surface area parameter (S_{BET}). It is also observed that S_{BET} correlate well with Raman and EIS parameters. Thus, we are tempted to ascribe the improved performances with improved charge transport properties[57,66] and densification effects.[41]

The previous investigations suggest that other uncounted effects may contribute as well, such as: nanoparticle spatial statistics, electrochemically active region of nanoparticles (affected

by Bi-O-Fe interactions) and macroscopic surface coverage of electrodes (influenced by CBi / CBiFe aggregate size distribution and deposition parameters). Advances are made towards quantifying these les accessible effects using electron microscopy (**Figure 11-3**). By following the image processing treatments described in **Chapter 10**, we suggest that SEM can be used to evaluate micro-scale variations in electrode modifications that i.e. may trace to the macroscopic surface coverage (Θ) of electrodes before and after their use in electrochemical experiments.

11.4 Hydrogen peroxide detection

During the experiments performed with CXBiFe materials with different Fe concentrations, H_2O_2 detection were evaluated by amperometry. One typical response curve is presented in **Figure 11-3a**. The measurements indicate fast stabilization time (~ below 6s) which serves as one advantage of the investigated systems. The results indicate that even though the Fe addition was proven to decrease the Pb^{2+} detection efficiency, H_2O_2 detection increases with Fe concentration in CXBiFe nanocomposites, while binary (CBiFe0 sample) systems did not show relevant activity.

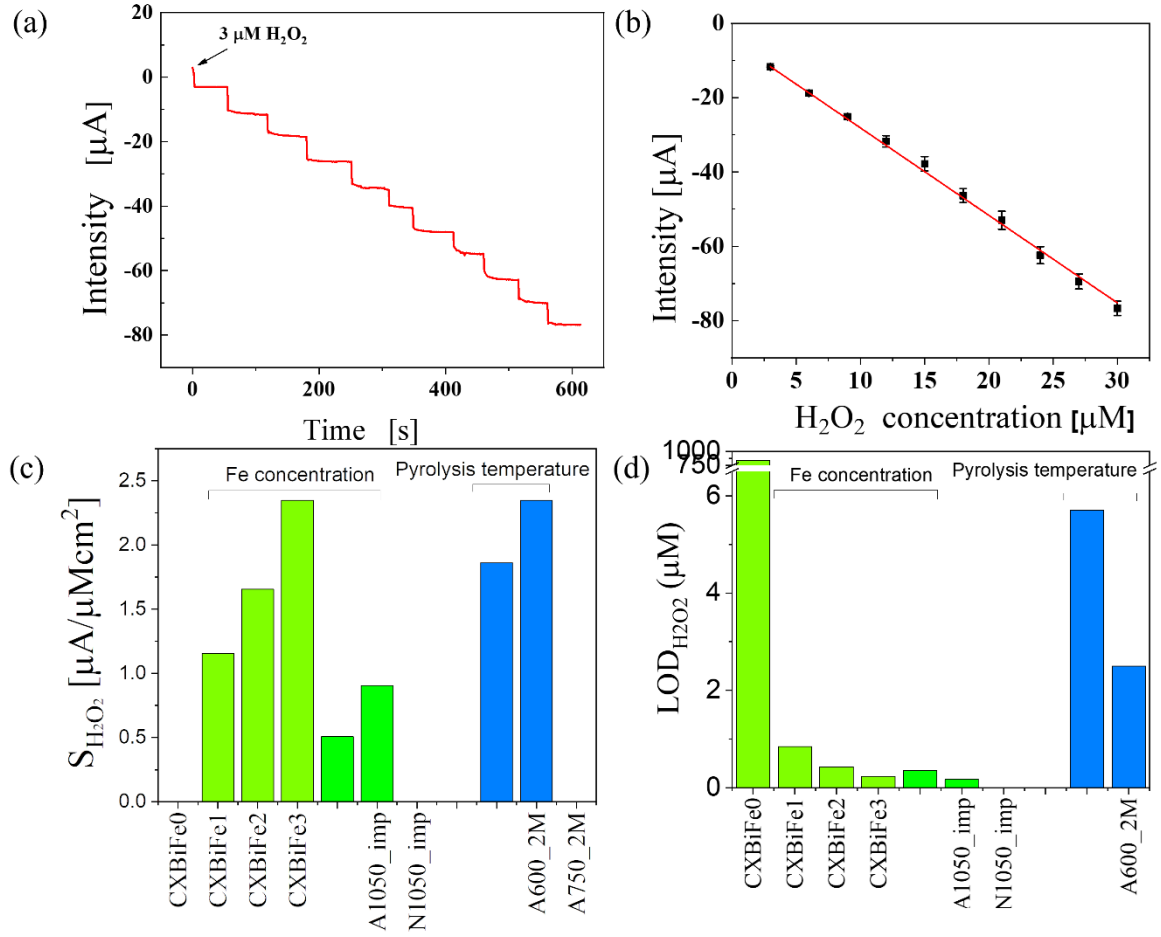

Figure 11-3. H_2O_2 detection at GC-chit-CXBiFe electrodes: (a) amperometric curve obtained for successive addition of 3 µM H_2O_2 (b) calibration curve, (c) H_2O_2 sensitivities and (d) LOD values obtained for different CBiFe modified electrodes under similar conditions and concentration ranges

A good correlation is observed between the initial Fe concentration, the EIS parameters and the LOD_{Pb2+}. The S_{H2O2} parameter shows a non-linear increase with Fe precursor concentration. The changes in the carbon support related with S_{BET} and I_D/I_G could not evidence any consistent

impact on the electrochemical parameters. The data does not exclude that interactions leading to BFO structures may be responsible for this non-linearity.

11.6 Conclusions

Binary CBi and ternary CBiFe nanocomposite xerogels and aerogels were electrochemically characterized and tested as electrode materials for heavy metal and bio-marker detection. It is proven that the ternary CBiFe systems hold multifunctional features as they detect both heavy metal and H_2O_2, with certain drawbacks since Bi-O-Fe interactions may decrease the overall performance. The correlation between the electrochemical and morpho-structural investigations support this claim. However, this may be, the results confirm that such materials have potential in detecting trace concentrations of both heavy metal and bio-markers. The high pyrolysis and nanocomposite processing as monolith leads to improved performances of CBiFe nanocomposites as temperature treatment will positively affect the systems at multiple scales. The study revealed a complex architecture that should be fully taken into account in the future in order to rigorously describe the electrochemical behavior and to further reach their full potential. The systems proved to be stable and robust. Low amounts of nanocomposites are necessary in order to obtain a workable electrode system. The use of noble metals, enzymes or more pretencious carbon materials such as carbon aerogels, nanotubes or graphenes can be avoided, therefore CBi and CBiFe xerogel solutions might also benefit from lower production costs.

12. Final conclusions and future work

General conclusions

The subject of the current thesis consists in the investigation of some nanocomposite electrode materials based on carbon gels (xerogels and aerogels) with embedded nanoparticles based on Bi and Fe (CBi and CBiFe) for electrochemical detection of heavy metals (i.e. Pb^{2+}, Cd^{2+}, etc.) and/or bio-markers (i.e. H_2O_2).

The type of drying (ambient drying versus supercritical drying) induces a dramatic change in the sample porosity, crystallinity and composition of the CBi and CBiFe nanocomposites. Coupled with the electrochemical analysis, it is concluded that an ambient drying is preferred both from the perspectives of higher electrochemical performances as well as lowering synthesis costs.

Iron introduced during co-synthesis or subsequent enrichment via an impregnation route enables the CBiFe nanocomposite to detect H_2O_2. This approach also leads to a compromise, as the presence of iron will negatively affect the heavy metal detection efficiency. Through TEM and STEM/EDX investigations, peculiar nanoparticles with a janus-like heterogeneous distribution of Bi and Fe phases is observed, suggesting that coverage of the electroactive surface (Bi) with iron oxide or bismuth iron oxide (mullite phase) would be the main reason for lowering the electrochemical performances.

The thermal evolution stages of the CBiFe composite (See **Figure 12-1**) is evidenced during the in situ TEM as follows: (1) precursor decomposition (~100-250 °C), (2) carbonization (~250-750 °C), (3) reduction (~600-800 °C) and (4) Fe assisted graphitization (~800-900 °C). Investigations on samples pyrolyzed at different conditions complement the in-situ TEM findings

with results specific to nano and micro-scales. The system is characterized as a nano-crystalline graphite (sizes below 5 nm) based microporous network that transits to a conductive state at the end of the carbonization stage (600-750 °C). With increasing temperatures (750-1050 °C), the nanocomposites exhibit a progressive compactization, nanoparticle reduction and splitting of the hybrid BFO nanoparticles as well as metal losses and delayed graphitization stage at high temperatures (900-1050 °C). Other parameters such as the CBiFe aggregate size and microscopic coverage defined as the ratio between nanoparticle size and the size of the Voronoi cells are also affected by pyrolysis and are highlighted as significant parameters in understanding the link between material parameters and electrochemical performances for later studies. Graphitization was evidenced after 1050 °C pyrolysis for one CBiFe xerogel sample found in enhanced graphitization stage (graphitic phase tending towards an interconnected network) and only in incipient graphitization stage/late reduction stage for other CBiFe samples even if they possessed higher graphitization catalyst concentrations. Due to these multi-scale effects, the final pyrolysis step was shown to greatly influence the electrochemical performances i.e. as seen during EIS analysis and SWASV detection of Pb^{2+}.

All in all, the investigated CBi and CBiFe xerogels and aerogels systems where shown to have potential for applications such as heavy metal detection, as Pb^{2+} concentrations in the range of 1-10 nM could be detected, well below the existing standards for safe drinking water. The best results were observed for the binary systems i.e. CBi xerogels with an intermediate pyrolysis temperature, but CBiFe nanocomposites exhibited multifunctional features due to their ability to detect Pb^{2+} as well as H_2O_2. The synthesis of CBi and CBiFe monoliths proved to be robust and may be potentially considered as starting material for future miniaturized electrodes.

Current limits and future work

As observed, the current thesis explores a complex interface between synthesis, material and electrochemical response, each domain having multiple variables that need be considered and further treated separately for a systematic approach. A work in progress furthers the understanding of high temperature, graphitized and ungraphitized CBiFe xerogels and aerogels and the transport and mobility of water molecules confined inside such networks. Another direction found in progress refers to improving the sample processing for the analysis of spatial distribution of phases in CBiFe nanocomposites at even larger scales. I hope that the overall results feed the quest for deeper perspectives in nanocomposite characterization and may contribute to the design of future sensors for heavy metal trace analysis not just for aqueous- but also for more complex environments. Based on the experience achieved during the present thesis, future work will expand towards the multiscale characterization of complex materials such as nanocomposites or hierarchic structures with impact towards environment and energy applications, where network related effects such as percolation phenomena require advanced characterization tools and a deeper understanding.

References

(1) *https://www.charitywater.org*. https://www.charitywater.org (accessed 2022-03-24).

(2) Geneva: World Health Organization. *Guidelines for Drinking-Water Quality: Fourth Edition Incorporating the First Addendum*; 2017.

(3) European Parliament and the Council. Directive 2013/35/EU. *National Primary Drinking Water Regulations Contaminant - Directive 2013/35/EU* **2009**, *1*.

(4) Gich, M.; Fernández-Sánchez, C.; Cotet, L. C.; Niu, P.; Roig, A. *Journal of Materials Chemistry A* **2013**, *1* (37), 11410–11418. https://doi.org/10.1039/c3ta12190a.

(5) Rusu, M. M.; Fort, C. I.; Cotet, L. C.; Vulpoi, A.; Todea, M.; Turdean, G. L.; Danciu, V.; Popescu, I. C.; Baia, L. *Sensors and Actuators B: Chemical* **2018**, *268*, 398–410. https://doi.org/10.1016/j.snb.2018.04.103.

(6) Fort, C. I.; Cotet, L. C.; Vulpoi, A.; Turdean, G. L.; Danciu, V.; Baia, L.; Popescu, I. C. *Sensors and Actuators B: Chemical* **2015**, *220*, 712–719. https://doi.org/10.1016/j.snb.2015.05.124.

(7) Fort, C. I.; Rusu, M. M.; Pop, L. C.; Cotet, L. C.; Vulpoi, A.; Baia, M.; Baia, L. *Journal of Nanoscience and Nanotechnology* **2021**, *21* (4), 2323–2333. https://doi.org/10.1166/jnn.2021.18963.

(8) Rusu, M. M.; Vulpoi, A.; Maurin, I.; Cotet, L. C.; Pop, L. C.; Fort, C. I.; Baia, M.; Baia, L.; Florea, I. *Microscopy and Microanalysis* **2022**, 1–13. https://doi.org/10.1017/S1431927622000241.

(9) Fort, C. I.; Rusu, M. M.; Cotet, L. C.; Vulpoi, A.; Florea, I.; Tuseau-Nenez, S.; Baia, M.; Baibarac, M.; Baia, L. *Molecules* **2021**, *26* (1), 117. https://doi.org/10.3390/molecules26010117.

(10) Švancara, I.; Prior, C.; Hočevar, S. B.; Wang, J. *Electroanalysis* **2010**, *22* (13), 1405–1420. https://doi.org/10.1002/elan.200970017.

(11) Tian, K.; Prestgard, M.; Tiwari, A. *Materials Science and Engineering: C* **2014**, *41*, 100–118. https://doi.org/https://doi.org/10.1016/j.msec.2014.04.013.

(12) Prieto-simo, B.; Armatas, G. S.; Pomonis, P. J.; Nanos, C. G.; Prodromidis, M. I. **2004**, No. 12, 1026–1034.

(13) Mani, V.; Devasenathipathy, R.; Chen, S. M.; Subramani, B.; Govindasamy, M. *International Journal of Electrochemical Science* **2015**, *10* (1), 691–700.

(14) Gholivand, M. B.; Torkashvand, M. *Materials Science & Engineering C* **2014**. https://doi.org/10.1016/j.msec.2014.12.003.

(15) Carrasco-Díaz, M. R.; Castillejos-López, E.; Cerpa-Naranjo, A.; Rojas-Cervantes, M. L. *Microporous and Mesoporous Materials* **2017**, *237* (January), 282–293. https://doi.org/10.1016/j.micromeso.2016.09.035.

(16) Hegedüs, A.; Erdei, S.; Horváth, G. *Plant Science* **2001**, *160* (6), 1085–1093. https://doi.org/10.1016/S0168-9452(01)00330-2.

(17) Vinodhini, R.; Narayanan, M. *Turkish Journal of Veterinary and Animal Sciences* **2009**, *33* (4), 273–278. https://doi.org/10.3906/vet-0711-18.

(18) Mushtakova, V. M.; Fomina, V. A.; Rogovin, V. v. *Izvestiia Akademii nauk. Seriia biologicheskaia / Rossiiskaia akademiia nauk* **2005**, *32* (3), 336–338.

(19) Flora, S. J. S.; Mittal, M.; Mehta, A. *Indian Journal of Medical Research* **2008**, *128* (4), 501–523.

(20) Fort, C. I.; Cotet, L. C.; Danciu, V.; Turdean, G. L.; Popescu, I. C. *Materials Chemistry and Physics* **2013**, *138* (2–3), 893–898. https://doi.org/10.1016/j.matchemphys.2012.12.079.

(21) Bollella, P.; Fusco, G.; Tortolini, C.; Sanzò, G.; Favero, G.; Gorton, L.; Antiochia, R. *Biosensors and Bioelectronics*. 2017. https://doi.org/10.1016/j.bios.2016.03.068.

(22) Pekala, R. W. *Journal of Materials Science* **1989**, *24* (9), 3221–3227. https://doi.org/10.1007/BF01139044.

(23) Pekala, R. W.; Alviso, C. T.; LeMay, J. D. *Journal of Non-Crystalline Solids* **1990**, *125* (1–2), 67–75. https://doi.org/10.1016/0022-3093(90)90324-F.

(24) Lu, X.; Caps, R.; Fricke, J.; Alviso, C. T.; Pekala, R. W. *Journal of Non-Crystalline Solids* **1995**, *188* (3), 226–234. https://doi.org/10.1016/0022-3093(95)00191-3.

(25) Fung, A. W. P.; Wang, Z. H.; Dresselhaus, M. S.; Dresselhaus, G.; Pekala, R. W.; Endo, M. *Physical Review B* **1994**, *49* (24), 17325–17335. https://doi.org/10.1103/PhysRevB.49.17325.

(26) Reynolds, G. A. M.; Fung, A. W. P.; Wang, Z. H.; Dresselhaus, M. S.; Pekala, R. W. *Journal of Non-Crystalline Solids* **1995**, *188* (1–2), 27–33. https://doi.org/10.1016/0022-3093(95)00029-1.

(27) Mayer, S. T.; Pekala, R. W.; Kaschmitter, J. L. *J Electrochem Soc* **1993**, *140* (2), 446–451. https://doi.org/10.1149/1.2221066.

(28) Pekala, R. W.; Farmer, J. C.; Alviso, C. T.; Tran, T. D.; Mayer, S. T.; Miller, J. M.; Dunn, B. *Journal of Non-Crystalline Solids* **1998**, *225* (1–3), 74–80. https://doi.org/10.1016/S0022-3093(98)00011-8.

(29) Miller, J. M.; Dunn, B.; Tran, T. D.; Pekala, R. W. *J Electrochem Soc* **1997**, *144* (12). https://doi.org/10.1149/1.1838142.

(30) Farmer, J. C.; Fix, D. v.; Mack, G. v.; Pekala, R. W.; Poco, J. F. *Journal of The Electrochemical Society* **1996**, *143* (1), 159–169. https://doi.org/10.1149/1.1836402.
(31) Farmer, J. C.; Fix, D. v; Pekala, R. W.; Nielsen, J. K.; Volpe, A. M. LAWRENCE LIVERMORE NATIONAL LAB CA, 1996.
(32) Moreno-Castilla, C.; Maldonado-Hódar, F. J. *Carbon N Y* **2005**, *43* (3), 455–465. https://doi.org/10.1016/j.carbon.2004.10.022.
(33) Kiciński, W.; Szala, M.; Cłapa, T.; Syczewski, M.; Borkowski, A. *Carbon N Y* **2018**, *127*, 479–490. https://doi.org/10.1016/j.carbon.2017.11.036.
(34) Sharma, C. S.; Katepalli, H.; Sharma, A.; Teixidor, G. T.; Madou, M. J. *ECS Transactions* **2014**, *61* (7), 45–54. https://doi.org/10.1149/06107.0045ecst.
(35) Sharma, C. S.; Verma, A.; Kulkarni, M. M.; Upadhyay, D. K.; Sharma, A. *ACS Applied Materials and Interfaces* **2010**, *2* (8), 2193–2197. https://doi.org/10.1021/am100512c.
(36) Hasegawa, G.; Shimizu, T.; Kanamori, K.; Maeno, A.; Kaji, H.; Nakanishi, K. *Chemistry of Materials* **2017**, *29* (5), 2122–2134. https://doi.org/10.1021/acs.chemmater.6b04706.
(37) Wang, X.; Lu, L.-L.; Yu, Z.-L.; Xu, X.-W.; Zheng, Y.-R.; Yu, S.-H. *Angewandte Chemie International Edition* **2015**, *54* (8), 2397–2401. https://doi.org/10.1002/anie.201410668.
(38) Lewicki, J. P.; Fox, C. A.; Worsley, M. A. *Polymer (Guildf)* **2015**, *69*, 45–51. https://doi.org/10.1016/j.polymer.2015.05.016.
(39) Al-Muhtaseb, S. A.; Ritter, J. A. *Advanced Materials* **2003**, *15* (2), 101–114. https://doi.org/10.1002/adma.200390020.
(40) Schaefer, D. W.; Pekala, R.; Beaucage, G. *Journal of Non-Crystalline Solids* **1995**, *186*, 159–167. https://doi.org/10.1016/0022-3093(95)00043-7.
(41) Maldonado-Hódar, F. J.; Moreno-Castilla, C.; Rivera-Utrilla, J.; Hanzawa, Y.; Yamada, Y. *Langmuir* **2000**, *16* (9), 4367–4373. https://doi.org/10.1021/la991080r.
(42) Wang, J.; Lu, J.; Hocevar, S. B.; Farias, P. A. M.; Ogorevc, B. *Analytical Chemistry* **2000**, *72* (14), 3218–3222. https://doi.org/10.1021/ac000108x.
(43) Serrano, N.; Alberich, A.; Díaz-Cruz, J. M.; Ariño, C.; Esteban, M. *TrAC Trends in Analytical Chemistry* **2013**, *46*, 15–29. https://doi.org/10.1016/J.TRAC.2013.01.012.
(44) Adekunle, A. S.; Agboola, B. O.; Pillay, J.; Ozoemena, K. I. *Sensors and Actuators, B: Chemical* **2010**, *148* (1), 93–102. https://doi.org/10.1016/j.snb.2010.03.088.
(45) Haghgoo, M.; Yousefi, A. A.; Mehr, M. J. Z.; Léonard, A. F.; Philippe, M. P.; Compère, P.; Léonard, A.; Job, N. *Journal of Materials Science* **2015**, *50* (18), 6007–6020. https://doi.org/10.1007/s10853-015-9148-0.
(46) Campbell, P. G.; Worsley, M. A.; Hiszpanski, A. M.; Baumann, T. F.; Biener, J. *Journal of Visualized Experiments* **2015**, No. 105, 3–9. https://doi.org/10.3791/53235.
(47) Weisweiler, W.; Subramanian, N.; Terwiesch, B. *Carbon N Y* **1971**, *9* (6). doi.org/10.1016/0008-6223(71)90008-X.
(48) Rouquerol, F.; Rouquerol, J.; Sing, K. S. W.; Maurin, G.; Llewellyn, P. (Second E., Eds.; Elsevier: Oxford, 2014; pp 1–24. https://doi.org/10.1016/B978-0-08-097035-6.00001-2.
(49) Ma, P.-C.; Siddiqui, N. A.; Marom, G.; Kim, J.-K. *Composites Part A: Applied Science and Manufacturing* **2010**, *41* (10), 1345–1367. https://doi.org/10.1016/j.compositesa.2010.07.003.
(50) Li, J.; Ma, P. C.; Chow, W. S.; To, C. K.; Tang, B. Z.; Kim, J. K. *Advanced Functional Materials* **2007**, *17* (16), 3207–3215. https://doi.org/10.1002/adfm.200700065.
(51) Snow, E. S.; Novak, J. P.; Campbell, P. M.; Park, D. *Applied Physics Letters* **2003**, *82* (13), 2145–2147. https://doi.org/10.1063/1.1564291.
(52) Schindelin, J.; Arganda-Carreras, I.; Frise, E.; Kaynig, V.; Longair, M.; Pietzsch, T.; Preibisch, S.; Rueden, C.; Saalfeld, S.; Schmid, B.; Tinevez, J.-Y.; White, D. J.; Hartenstein, V.; Eliceiri, K.; Tomancak, P.; Cardona, A. *Nature Methods* **2012**, *9* (7), 676–682. https://doi.org/10.1038/nmeth.2019.
(53) Kharlamova, M. v. Investigation of Growth Dynamics of Carbon Nanotubes. **2017**, 826–856. https://doi.org/10.3762/bjnano.8.85.
(54) van de Burgt, Y.; Bellouard, Y.; Mandamparambil, R. *Physical Chemistry Chemical Physics* **2014**, *16* (11), 5162–5173. https://doi.org/10.1039/c4cp00061g.
(55) Althea, G.; Reynolds, M. Electronic Transport and Photoconductive Properties of Resorcinol-Formaldehyde-Based Carbon Aerogels, MIT PhD Thesis, **1995**.
(56) Czigány, Z.; Hultman, L. *Ultramicroscopy* **2010**, *110* (7), 815–819. https://doi.org/10.1016/j.ultramic.2010.02.005.
(57) Najeh, I.; ben Mansour, N.; Dahman, H.; Alyamani, A.; el Mir, L. *Journal of Physics and Chemistry of Solids* **2012**, *73* (6), 707–712. https://doi.org/10.1016/j.jpcs.2011.12.007.
(58) Merlen, A.; Buijnsters, J.; Pardanaud, C.; Gerardus Buijnsters, J. *Coatings* **2017**, *7* (10), 153. https://doi.org/10.3390/coatings7100153ï.

(59) Ferrari, A. C.; Robertson, J. *Philosophical Transactions of the Royal Society of London. Series A: Mathematical, Physical and Engineering Sciences* **2004**, *362* (1824), 2477–2512. https://doi.org/10.1098/rsta.2004.1452.
(60) Guenther, G.; Theissmann, R.; Guillon, O. *The Journal of Physical Chemistry C* **2014**, *118* (46), 27020–27027. https://doi.org/10.1021/jp509841s.
(61) Lu, J.; Qiao, L. J.; Fu, P. Z.; Wu, Y. C. *Journal of Crystal Growth* **2011**, *318* (1), 936–941. https://doi.org/10.1016/j.jcrysgro.2010.10.181.
(62) Compton, R. G.; Banks, C. E. *Understanding Voltammetry*; IMPERIAL COLLEGE PRESS, 2010. https://doi.org/10.1142/p726.
(63) Ward Jones, S. E.; Chevallier, F. G.; Paddon, C. A.; Compton, R. G. *Analytical Chemistry* **2007**, *79* (11), 4110–4119. https://doi.org/10.1021/ac070046b.
(64) Testa-Anta, M.; Ramos-Docampo, M. A.; Comesaña-Hermo, M.; Rivas-Murias, B.; Salgueiriño, V. *Nanoscale Advances* **2019**, *1* (6), 2086–2103. https://doi.org/10.1039/c9na00064j.
(65) Shebanova, O. N.; Lazor, P. *Journal of Raman Spectroscopy* **2003**, *34* (11), 845–852. https://doi.org/10.1002/jrs.1056.
(66) Najeh, I.; Mansour, N. B. E. N.; Dahman, H.; Alyamani, A.; Mir, L. E. L. *Sensors & Transducers* **2014**, *27* (May), 285–289.

Thesis related publication list

(1) **Rusu, M. M**.; Fort, C. I.; Cotet, L. C.; Vulpoi, A.; Todea, M.; Turdean, G. L.; Danciu, V.; Popescu, I. C.; Baia, L. Insights into the Morphological and Structural Particularities of Highly Sensitive Porous Bismuth-Carbon Nanocomposites Based Electrochemical Sensors. *Sensors and Actuators B: Chemical* **2018**, *268*, 398–410. https://doi.org/10.1016/j.snb.2018.04.103. (AIS = 0.8)

(2) Fort, C. I.; **Rusu, M. M**.; Pop, L. C.; Cotet, L. C.; Vulpoi, A.; Baia, M.; Baia, L. Preparation and Characterization of Carbon Xerogel Based Composites for Electrochemical Sensing and Photocatalytic Degradation. *Journal of Nanoscience and Nanotechnology* **2021**, *21* (4), 2323–2333. https://doi.org/10.1166/jnn.2021.18963. (AIS = 0.142)

(3) Fort, C. I.; **Rusu, M. M**.; Cotet, L. C.; Vulpoi, A.; Florea, I.; Tuseau-Nenez, S.; Baia, M.; Baibarac, M.; Baia, L. Carbon Xerogel Nanostructures with Integrated Bi and Fe Components for Hydrogen Peroxide and Heavy Metal Detection. *Molecules* **2021**, *26* (1), 117. https://doi.org/10.3390/molecules26010117. (AIS = 0.694)

(4) **Rusu, M. M**.; Vulpoi, A.; Maurin, I.; Cotet, L. C.; Pop, L. C.; Fort, C. I.; Baia, M.; Baia, L.; Florea, I. Thermal Evolution of C–Fe–Bi Nanocomposite System: From Nanoparticle Formation to Heterogeneous Graphitization Stage. *Microscopy and Microanalysis* **2022**, 1–13. https://doi.org/10.1017/S1431927622000241. (AIS = 0.968)

Patents related to the subject of the thesis:

Coteț L.C., Baia L. G., Forț C.I., Pop L.C., Rusu M. M. – Procedeu de obținere a materialelor compozite de tipul carbon nanoporos/grafen/nanoparticule de bismut și fier/ oxide de titan cu proprietăți analitice și de fotodegradare, A 2017 00826, RO 133255 A2, accepted in 2020.

Other publications:

(5) **Rusu, M. M.**; Wahyuono, R. A.; Fort, C. I.; Dellith, A.; Dellith, J.; Ignaszak, A.; Vulpoi, A.; Danciu, V.; Dietzek, B.; Baia, L. Impact of Drying Procedure on the Morphology and Structure of TiO_2 Xerogels and the Performance of Dye Sensitized Solar Cells. *Journal of Sol-Gel Science and Technology* **2017**, *81* (3). https://doi.org/10.1007/s10971-016-4237-3.

(6) Tarcan, R.; Handrea-Dragan, M.; Todor-Boer, O.; Petrovai, I.; Farcau, C.; **Rusu, M.**; Vulpoi, A.; Todea, M.; Astilean, S.; Botiz, I. A New, Fast and Facile Synthesis Method for Reduced Graphene Oxide in N,N-Dimethylformamide. *Synthetic Metals* **2020**, *269*. https://doi.org/10.1016/j.synthmet.2020.116576.

(7) Anghel, I.; Lisa, G.; Șofran, I.-E.; Mitroi-Symeonidis, F.-C.; **Rusu, M. M.**; Baia, M.; Baia, L.; Magyari, K.; Danciu, V.; Cotet, L. C.; Stroe, M.; Baibarac, M. Pyrolysis and Combustion of Polystyrene Composites Based on Graphene Oxide Functionalized with 3-(Methacryloyloxy)-Propyltrimethoxysilane. *Journal of Polymer Engineering* **2021**. https://doi.org/10.1515/polyeng-2021-0071.

(8) Todea, M.; Simon, V.; Muresan-Pop, M.; Vulpoi, A.; **Rusu, M. M**.; Simion, A.; Vasilescu, M.; Damian, G.; Petrisor, D. M.; Simon, S. Silica-Based Microspheres with Aluminum-Iron Oxide Shell for Diagnosis and Cancer Treatment. *Journal of Molecular Structure* **2021**, *1246*, 131149. https://doi.org/10.1016/j.molstruc.2021.131149.

(9) Suarasan, S.; Tira, C.; **Rusu, M. M.**; Craciun, A.-M.; Focsan, M. Controlled Fluorescence Manipulation by Core-Shell Multilayer of Spherical Gold Nanoparticles: Theoretical and Experimental Evaluation. *Journal of Molecular Structure* **2021**, *1244*, 130950. https://doi.org/10.1016/j.molstruc.2021.130950.

Participation at scientific conferences

(1) **Rusu M. M.**; Florea I.; Vulpoi A.; Baia L.; Ardelean I. Investigating phenomena in porous composite materials: from the setting of cement pastes to the pyrolysis of CBiFe xerogels, BRAMAT, 2022, Brașov, Romania. (**Oral Presentation**)

(2) **Rusu M. M.**; Vulpoi A., Fort C.I.; Cotet L.C.; Florea I.; Baia M.; Baia L. Characterization of nanocomposite xerogel systems based on carbon, bismuth and iron, CSDC-MIF, 2020, Iași, Romania (**Oral Presentation**)

(3) **Rusu M. M**.; Vulpoi A., Fort C.I.; Cotet L.C.; Baia M.; Baia L. An attempt to understand heavy metal deposition processes on electrodes modified with C-Bi nanocomposites using electron microscopies, CREMS, 2019, Poiana Brașov, Romania **(Poster)**

(4) **Rusu M. M**.; Vulpoi A., Fort C.I.; Cotet L.C.; Baia M.; Baia L. Composite materials based on Bi-Fe nanoparticles / Carbon Xerogel with environmental analytical applications, ICPAM-PAMS, 2016, Cluj-Napoca, Romania **(Poster)**

(5) **Rusu M. M**.; Cotolan N.; Lazar A.; Fort C.I. Baia L.; Cotet L.C. In situ preparation of Graphene/Porous Carbon/Bi-Fe nanoparticle heterostructures for analytical applications, Graphene Week, 2016, Warsaw, Poland **(Poster)**

National Awards

First prize at the "Mircea Stoian" Scientific Paper Competition, 2019 (second edition) for the article entitled "Insights into the Morphological and Structural Particularities of Highly Sensitive Porous Bismuth-Carbon Nanocomposites Based Electrochemical Sensors", Sensors and Actuators B: Chemical.